metals

MDPI

Article

Elastoplastic Deformation of Rotating Disk Made of Aluminum Dispersion-Hardened Alloys

Oleg Matvienko [1,2], Olga Daneyko [1,2], Vladimir Valikhov [1,*], Vladimir Platov [1], Ilya Zhukov [1] and Aleksandr Vorozhtsov [1]

[1] Faculty of Physics and Engineering, National Research Tomsk State University, 634050 Tomsk, Russia; matvolegv@mail.ru (O.M.); olya_dan@mail.ru (O.D.); vova.platov.85@mail.ru (V.P.); gofra930@gmail.com (I.Z.); abv@mail.tomsknet.ru (A.V.)

[2] General Education Faculty, Tomsk State University of Architecture and Building, 634003 Tomsk, Russia

* Correspondence: valihov.snobls@gmail.com

Abstract: This paper studies the plastic deformation of a rotating disk made of aluminum dispersion-hardened alloys using mechanical tensile tests and a structured study using optical microscopy methods. Alloys such as AA5056 and A356 with dispersed Al_3Er and TiB_2 particles are used as the initial materials. Tensile strength testing of the obtained alloys shows that the addition of Al_3Er particles in the AA5056 alloy composition leads to an increase in its ultimate stress limit (USL) and plasticity from 170 to 204 MPa and from 14.7 to 21%, respectively, although the modifying effect is not observed during crystallization. The addition of TiB_2 particles to the A356 alloy composition also leads to a simultaneous increase in the yield strength, USL, and plasticity from 102 to 145 MPa, from 204 to 263 MPa, and from 2.3 to 2.8%, respectively. The study of the stress-strain state of the disk was carried out in the framework of deformed solid mechanics. The equilibrium equations were integrated analytically, taking into account the hardening conditions obtained from the experimental investigations. This made it possible to write the analytical relations for the radial and circumferential stresses and to determine the conditions of plastic deformation and loss of strength. The plastic resistance of a disk depends on the ratio between its outer and inner radii. The plastic resistance decreases with increasing disk width at a constant inner radius, which is associated with a stronger effect from the centrifugal force field. At a higher rotational rate of narrow disks, the tangential stresses are high and can exceed the USL value. A356 and A356–TiB_2 alloys are more brittle than the AA5056 and AA5056–Al_3Er alloys. In the case of wide rotating disks, AA5056 and AA5056–Al_3Er alloys are preferable.

Keywords: rotating disk; stress-strain state; dispersion-hardened materials; nanoparticles; strain hardening; plastic strain; mathematical model

check for updates

Citation: Matvienko, O.; Daneyko, O.; Valikhov, V.; Platov, V.; Zhukov, I.; Vorozhtsov, A. Elastoplastic Deformation of Rotating Disk Made of Aluminum Dispersion-Hardened Alloys. *Metals* **2023**, *13*, 1028. https://doi.org/10.3390/met13061028

Academic Editors: Zhengyi Jiang and Hongmei Zhang

Received: 26 April 2023
Revised: 16 May 2023
Accepted: 23 May 2023
Published: 27 May 2023

Copyright: © 2023 by the authors. Licensee MDPI, Basel, Switzerland. This article is an open access article distributed under the terms and conditions of the Creative Commons Attribution (CC BY) license (https://creativecommons.org/licenses/by/4.0/).

1. Introduction

The improvement of process facility performance requires the creation of materials that provide the appropriate levels of reliability and life. Such materials must possess high strength and sufficient plastic potential. In order to achieve these goals, it is advisable to utilize composite materials consisting of high-strength fillers (dispersed phases) and plastic binders (matrices).

According to Matthews and Rawlings [1], dispersion-hardened materials with nanoparticles in their matrix are of particular interest. These alloys manifest unique properties compared to conventional alloys. Unlike reinforced and laminated materials, the main advantages of dispersion-hardened alloys are the isotropy of mechanical properties, high plasticity, and strength [2,3]. Compared to fibers, dispersion-hardened composite materials are characterized by a load-bearing matrix. An ensemble of dispersed particles strengthens the material due to its resistance to dislocation motion under loading [4]. This hinders

plastic deformation and improves the strength and stress–strain properties of materials. Since the strength properties of dispersion-hardened materials depend on the particle shape and size, a variation in the matrix composition, particle size, and volume fraction makes it possible to create materials with the required properties. Kröpfl et al. [5] considered the deformation process in dispersion-hardened aluminum materials during uniaxial creep in a wide temperature range. It was found that the yield strength was significantly reduced at elevated temperatures. Stobrawa et al. [6] reported a considerable improvement in the properties of nanoparticle-strengthened composites.

The addition of strengthening particles greatly increases the mechanical properties (ultimate stress limit and hardness) and performance (wear resistance) of materials [7]. Dispersion-hardened metallic materials demonstrate an excellent strength/plasticity ratio. According to [8], a wide range of materials with the required property set can be obtained by changing the matrix, particle size, and volume fraction. The modification of these parameters provides a wide spectrum of materials with the required property set [9].

The use of nonmetallic particles is a promising technique to improve the structures of cast alloys. There are currently a number of experimental data on the use of metal oxides (Al_2O_3, TiO_2), carbides, and borides for the grain structure modification of Al–Si alloys [10–14].

In our early research [15], we studied the microstructure and mechanical properties of the aluminum alloy A356 strengthened by the scandium trifluoride (ScF_3) nanoparticles with a negative thermal expansion coefficient. The alloy demonstrated a highly efficient use of ScF_3-based modifiers and additional ultrasonic treatment. The mechanical mixing and vibration treatment used in [16] affected the structure and mechanical properties of the aluminum alloy A356–C consisting of $\leq$1 wt.% nanodiamonds. It was shown that the yield strength and ultimate stress limit (USL) of the A356 alloy increased without changing its plasticity. In [17], we conducted an integrated study of the alloy production process and the treatment effect on its physical and mechanical properties. It was found that the grain structure of the alloys consisting of TiB_2 particles was completely formed. The addition of TiB_2 particles increased the yield strength, USL, and plasticity of the alloys. The highest effect from the ground structure of the cast alloys was achieved by using a master alloy consisting of 1 μm TiB_2 particles.

As shown in [18], the strength properties of dispersion-hardened materials depend on the particle shape and size, strain temperature, and rate. Alloy strengthening depends on the particle type, volume fraction, and particle distribution in the matrix. Aluminum-based composites strengthened with particles are used in automobile construction, the construction industry, and aircraft engineering.

The plastic shear and strain hardening of heterophased alloys were studied by Orowan, Ashby, Hirsch [19–29], and others. It was found that the strain hardening of materials with nanoscale and nanodispersed strengthening phases independent of the matrix interface was more intensive than that of the materials with coarse particles at the same volume fraction of the strengthening phase.

The stress–strain state of copper pipe walls subjected to elastoplastic deformation was investigated in [30–32] by using the flow plasticity model combined with solid mechanics modeling.

Rotating disks are the most important elements in many mechanisms and devices [33–36]. Disk strength determines the high performance and lifetime of the mechanisms. Most of the up-to-date turbo-machines are provided with disks operating at higher loads, causing plastic deformation. These loads are mostly centrifugal forces induced by the rotation process. Due to the increased requirements for the safety and efficiency of up-to-date turbo-machines, it is necessary to develop new methods of investigating stress–strain states. In addition to solid disks, annular disks are used to study the stress–strain state of turbo-machine parts. This is also relevant for disks that are separately attached to a shaft.

The stress analysis of rotating disks and shafts is a classical problem in solid mechanics. Many studies are devoted to solving these problems using various methods [37–39]. Analytical solutions to the rotating disk problem are common in classical works devoted to theories of elasticity [40] and plasticity [41,42]. This problem is also discussed in many engineering studies. The simplest analytical modeling and preliminary design involve the use of a uniform solid or annular disk with a constant thickness subjected to one external centrifugal force. Most of the previous studies considered the Tresca–Saint Venant criterion and the material hardening conditions [43]. Another popular approach to this issue, proposed by Jahromi et al. [44], is the use of the von Mises yield criterion.

Apatay and Eraslan [45] suggested analytical solutions in terms of hypergeometric functions for the elastic deformation of rotating parabolic discs made of isotropic and homogeneous materials. Theoretical studies in [46] were used to investigate the stress–strain state of rotating hyperbolic disks fabricated from isotropic and homogeneous materials subjected to variable thermal loads. Using Tresca's yield condition, Güven [47] investigated a linearly hardening rotating solid disk with variable thickness. A theoretical stress analysis was given in [48] for rotating hyperbolic disks made of isotropic and homogeneous materials. Using Tresca's yield condition, Eraslan [49] suggested analytical solutions for stress distribution in rotating parabolic solid disks also made of an isotropic and homogeneous material with linear strain hardening. It was shown that the deformation behavior of a parabolic convex disk was similar to that of a uniform disk of the same thickness, but in the case of a parabolic concave disk, it was different. Based on Tresca's yield condition, the associated plastic flow rule, and linear material hardening, Eraslan [50] suggested an analytical solution for the elastic–plastic deformation of rotating parabolic disks under pressurized and radially constrained boundary conditions.

Vebil Yildirim [51] conducted a parametric study on the centrifugal force-induced stress and displacements in power-law graded hyperbolic discs, depending on inhomogeneity, profile, and boundary conditions. The radial thickness of the discs was selected such that it was governed by the hyperbolic function determined by either the convergent or divergent function.

Seth's transition theory was used in [52] to analyze elastoplastic stresses in a thin rotating disk with inclusion and edge loading. The obtained results could be used for both compressible and incompressible materials. It was found that at a high rotational rate of a loaded disk, it was necessary to account for material compressibility.

In terms of continuum mechanics, Aleksandrova et al. [53,54] considered the stress–strain state of a rotating disk with a constant thickness. The disk material was assumed to be homogeneous, elastic, and ideally plastic. A continuum-level solution was obtained for both the stresses and radial displacement using the von Mises yield criterion and the related plastic flow rule. In [55], a complete solution was suggested for practical engineering applications.

Afsar and Go [56] presented the finite element analysis of a thermoelastic field in a rotating thin circular disk with a concentric hole under a thermal load. The solution was obtained in [57] for a disk with a uniform thickness with regard to centrifugal forces and compressive stress.

The aim of this study is to determine the plastic deformation conditions for a rotating disk made of dispersion-hardened aluminum alloys, as illustrated in Figure 1.

In order to calculate stresses in the disk material, we used the approach described in detail in [58–61]. Based on this approach, stresses in the disk material were calculated using solid mechanics equations [62–65].

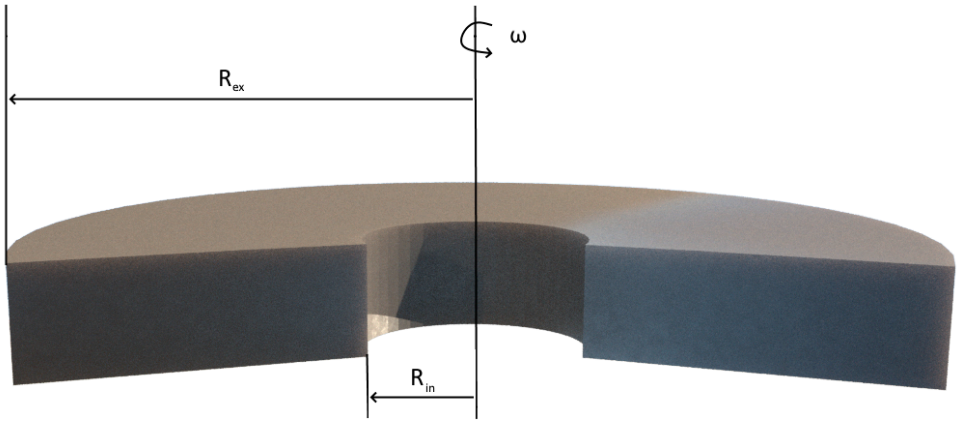

Figure 1. 3D view of uniform disk profiles.

2. Experimental Procedure and Results

2.1. AA5056–Al3Er Alloy

The aluminum alloy AA5056 (91.9–94.68% Al, 4.8–5.8% Mg) was used as the initial material. The Al–Al_3Er master alloy was obtained by erbium (Er) hydrogenation in a chemical reactor with successive mixing with Al micropowder, compaction, and dehydrogenation in a vacuum furnace. A total of 1 kg of the AA5056 alloy was placed in a crucible and molted in a muffle furnace at 780 °C for 2 h. When the crucible was removed from the furnace, the Al–Al_3Er master alloy was introduced into the melt via simultaneous ultrasonic treatment at a temperature of 730 °C. The ultrasonic treatment was performed using a magnetostriction water-cooling actuator at 4.1 kV voltage and 17.6 kHz frequency. After the complete dissolution of the master alloy, the melt was ultrasonically treated for 2 min. The melt was cast in a mold at 720 °C and underwent vibration treatment until complete crystallization. The initial AA5056 alloy was obtained under the same conditions but without the master alloy.

2.2. A356–TiB_2 Alloy

The aluminum alloy A356 (Al base metal, 6.9% Si, 0.339% Mg, 0.136% Ti, 0.124% Fe, and <0.05% other elements) was used as the initial material. Titanium diboride (TiB_2) particles were used to modify the alloy structure. The particle introduction and distribution in the A356 melt were performed by using master alloys with 60 wt.% Al and 40 wt.% TiB_2 obtained by gas-free burning of a mixture of aluminum, titanium, and boron powders [66]. The alloy was fabricated by melting 1 kg of the A356 alloy in a crucible at 750 °C for at least 4 h in a closed furnace. Master alloys were incorporated at 730 °C and mixed in a mechanical mixer [67] for 1 min in an open furnace. In order to reduce the porosity, obtain a homogeneous structure, and improve the distribution of alloying elements in the melt, vibration treatment was applied during 700 °C casting into the crucible. Vibration was conducted at a frequency of 60 Hz and 0.5 mm amplitude. An alloy without TiB_2 particles was created under the same conditions for comparison.

2.3. Methods

The metallographic analysis of the grain structure was conducted using an Olympus GX71 Inverted Microscope (Olympus, Tokyo, Japan). The alloy surface was then mechanically polished. Uniaxial tensile tests were carried out on an Instron 3369 Dual Column Tabletop Testing System (Instron, Norwood, MA, USA) at a 0.2 mm/min strain rate.

As can be seen in Figure 2a, the average grain size of the AA5056 alloy is 390 μm. The diffusion of Al3Er particles does not modify the alloy structure, and the average grain size is 410 μm, as shown in Figure 2b.

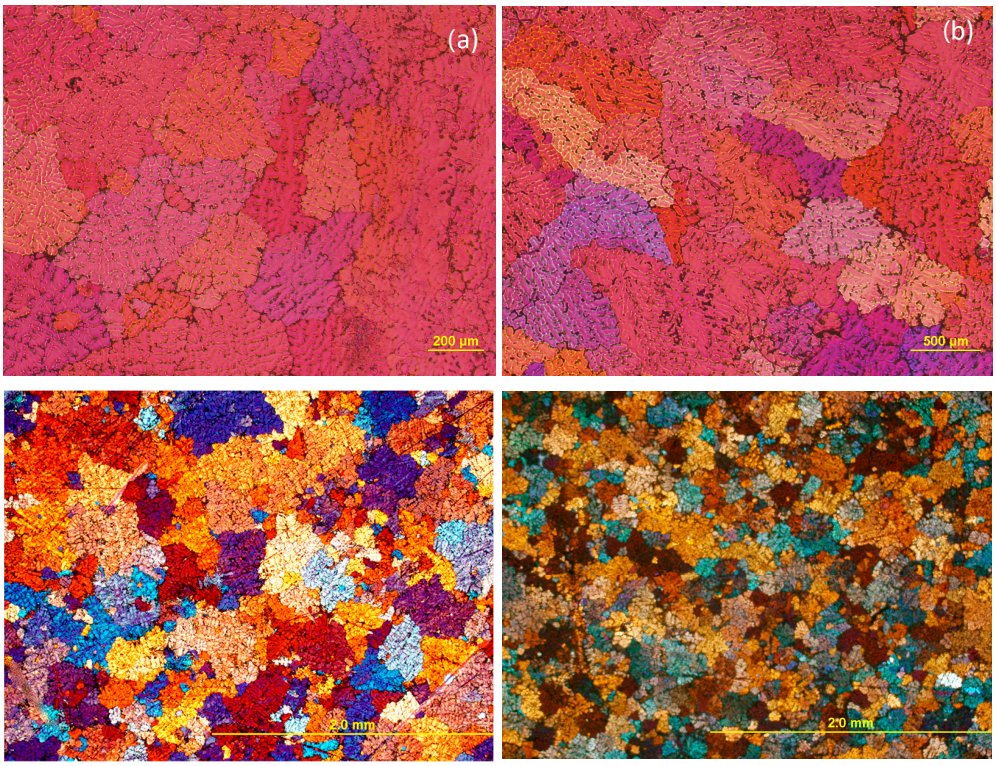

(**c**) (**d**)

Figure 2. Grain structure of different alloys. (**a**) AA5056; (**b**) AA5056–Al_3Er; (**c**) A356; (**d**) A356–TiB_2.

For the A356 alloy, the TiB_2 particle diffusion decreases the average grain size from 180 to 140 µm due to the formation of new crystallization centers on the particle surface. Due to the structural proximity of TiB_2 and Al crystals, titanium diboride is an effective nucleation center in the Al melt, which, in turn, leads to the formation of the fine structure of ingots. Based on the data obtained, it can be assumed that the modified aggregative state (crystallization) of the introduced (nano- or submicron-sized) particle surface has a significant effect on the grain size of the fabricated alloys. This is associated with the low-stability state of the melt–particle system, which provides a weak thermal effect from the inoculator microparticles on the final state of the alloy, namely, its structure and physical/mechanical properties. After the thermal interaction between the particles and the melt, the temperature of which approaches crystallization, the alloy crystallizes on the particle surface.

Tensile strength testing of the fabricated AA5056 alloy (see Figure 3, Table 1) shows that the introduction of Al_3Er particles into the melt improves the USL and plasticity from 170 to 204 MPa and from 14.7 to 21%, respectively, despite the absence of the modifying effect during crystallization. This effect is achieved through the introduction of Al_3Er particles, which contribute to the deflection of the potential crack from the grain boundaries into its volume, as well as increase the role of the aluminum matrix in the deformation and fracture processes. The TiB_2 particle diffusion in the A356 alloy also leads to a simultaneous increase in the yield strength, USL, and plasticity from 102 to 145 MPa, from 204 to 263, and from 2.3 to 2.8%, respectively.

The approximation of the experimental stress–strain curve allows us to obtain the function of $\sigma(\varepsilon)$ with an error not exceeding 0.1%:

$$\sigma = \begin{cases} \Gamma_{\text{eff}} \sigma_{0.2}^{(n-1)/n} \varepsilon, & \text{if} \quad \varepsilon \leq \left(\sigma_{0.2}/\Gamma_{\text{eff}}\right)^{1/n} \\ \Gamma_{\text{eff}} \varepsilon^n, & \text{if} \quad \left(\sigma_{0.2}/\Gamma_{\text{eff}}\right)^{1/n} < \varepsilon \end{cases} \tag{1}$$

where Γ_{eff} is the effective modulus of plasticity and n is the non-linearity parameter.

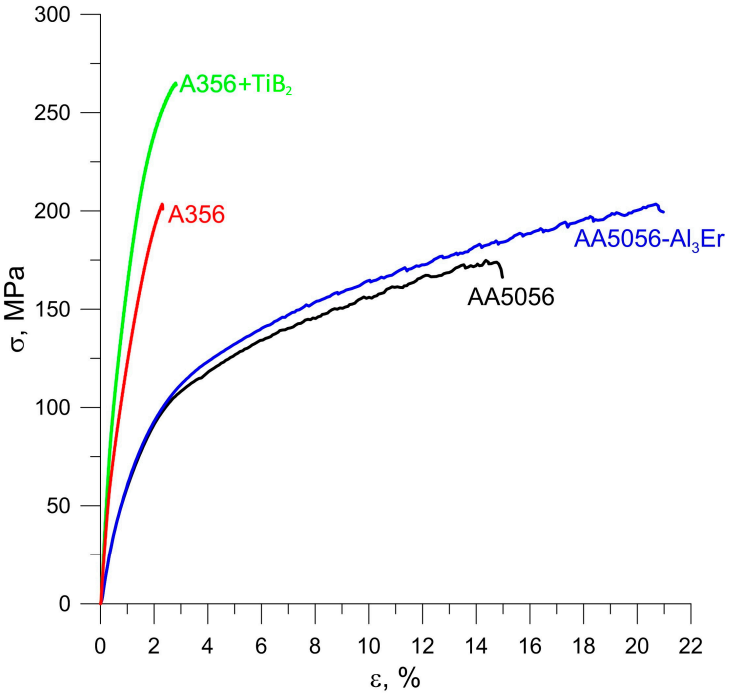

Figure 3. Loading diagrams of AA5056, AA5056–Al_3Er, A356, and A356–TiB_2 alloys.

Table 1. Parameters of initial and fabricated alloys.

Materials	$\sigma_{0.2}$, MPa	σ_B, MPa	ε_{max},%	G, GPa	ρ, g/cm^3	ν
A356	102	204	2.3	27.2 [68]	2.66 [69]	0.33 [70]
A356–0.5TiB_2	145	263	2.8	-	-	-
TiB_2	-	-	-	250 [71]	4.52 [72]	0.11 [73]
AA5056	63	170	14.75	27 [74]	2.65 [75]	0.34 [76]
AA5056–Al_3Er	64	204	21.37	-	-	-
Al_3Er		-	-	118 [77]	5.55 [78]	0.188 [79]

Parameters Γ_{eff} and n for different alloys are summarized in Table 2.

Table 2. Material constants: Γ_{eff} and n (1).

Alloys	Γ_{eff} [MPa]	n
A356	1762	0.52
A356–0.5TiB_2	2580	0.66
AA5056	343	0.34
AA5056–Al_3Er	314	0.30

3. Mathematical Model

Let us consider the stress–strain state of the thin disk induced by its rotation at a constant rotational rate ω. The gravity force effect on the stress–strain state is neglected. The proposed mathematical model is based on balance equations, which take the following form in the cylindrical system of coordinates [80]:

$$\frac{\partial \sigma_{rr}}{\partial r} + \frac{1}{r}\frac{\partial \sigma_{r\varphi}}{\partial \varphi} + \frac{\partial \sigma_{rz}}{\partial z} + \frac{\sigma_{rr} - \sigma_{\varphi\varphi}}{r} + \rho\omega^2 r = 0 \quad (2)$$

$$\frac{\partial \sigma_{r\varphi}}{\partial r} + \frac{1}{r}\frac{\partial \sigma_{\varphi\varphi}}{\partial \varphi} + \frac{\partial \sigma_{\varphi z}}{\partial z} + 2\frac{\sigma_{r\varphi}}{r} = 0 \tag{3}$$

$$\frac{\partial \sigma_{rz}}{\partial r} + \frac{1}{r}\frac{\partial \sigma_{\varphi z}}{\partial \varphi} + \frac{\partial \sigma_{zz}}{\partial z} = 0 \tag{4}$$

The system of Equations (2)–(4) can be simplified using the following assumptions. Since this problem is axially symmetric (the symmetry relative to one and the same axis is a deformed solid contour and lading conditions), normal stresses do not depend on the angular coordinate φ, and circumferential displacement and tangential stress are zero, viz. $u_\varphi = 0$, $\sigma_{r\varphi} = 0$, $\sigma_{\varphi z} = 0$. Therefore, (2) is identically satisfied.

We consider that the centrifugal force appearing during the disk rotation distributes symmetrically relative to the middle disk surface. If the disk base is free from external forces, the following conditions must be applied to it:

$$z = \pm H \tag{5}$$

With respect to (4) and (5), we can conclude that at $z = \pm H$, not only σ_{zz} becomes zero but so does its derivative $\frac{\partial \sigma_{zz}}{\partial z}$. On the strength of the symmetry conditions, in the center section, the axial shift and radial motion u_r on the axial coordinate are both zero, i.e., $u_z = 0$ and $\frac{\partial u_r}{\partial z} = 0$, respectively. Therefore, at rather low disk thickness, σ_{zz} and σ_{rz} stresses are small. Thus, it can be considered that these stresses are zero throughout the disk, whereas the radial motion depends on the radial coordinate $u_r = u_r(r)$ only.

In the thin disk, the plane state is implemented approximately. It is enough to use (2) to describe the plane state, which takes the form as follows:

$$\frac{\partial \sigma_{rr}}{\partial r} + \frac{\sigma_{rr} - \sigma_{\varphi\varphi}}{r} + \rho\omega^2 r = 0 \tag{6}$$

Next, we formulated the boundary conditions for (6). The pressure onto the inner and outer walls of the disk is suggested to be absent. Therefore, the boundary conditions are as follows:

$$r = R_{\text{in}}\colon\ \sigma_{rr} = 0, \quad r = R_{\text{ex}}\colon\ \sigma_{rr} = 0 \tag{7}$$

Equation (6) contains two unknown values, namely, σ_{rr} and $\sigma_{\varphi\varphi}$ stress tensor components. The additional relation for elastic deformation can be obtained from the equation of strain compatibility, which in the plane state takes the form as follows:

$$\frac{\partial \varepsilon_{\varphi\varphi}}{\partial r} - \frac{\varepsilon_{rr} - \varepsilon_{\varphi\varphi}}{r} = 0 \tag{8}$$

During the plastic deformation of the hardening medium, an additional condition, which links the stress tensor components, is plastic strain hardening [80]:

$$\max\left[\left|\sigma_{rr} - \sigma_{\varphi\varphi}\right|,\ \left|\sigma_{\varphi\varphi} - \sigma_{zz}\right|, \left|\sigma_{zz} - \sigma_{rr}\right|\right] \geq \sigma_{0.2} \tag{9}$$

The strength analysis of the disk is the most important task of calculating its stress–strain state. According to the maximum shear theory (Saint Venant's theory), material disintegration occurs due to the shear that is induced by tangential stresses [81]. This theory is well-proven for plastic materials, which resist equally to tension and compression. It is assumed that the material fracture occurs when the highest tangential stress achieves the limit value. In this case, the strength condition takes the following form [82,83]:

$$\max\left[\left|\sigma_{rr} - \sigma_{\varphi\varphi}\right|,\ \left|\sigma_{\varphi\varphi} - \sigma_{zz}\right|, \left|\sigma_{zz} - \sigma_{rr}\right|\right] \geq \sigma_B \tag{10}$$

Strain tensor components are determined by Cauchy relations and, in our case, they are determined as follows:

$$\varepsilon_{rr} = \frac{\partial u_r}{\partial r},\ \varepsilon_{zz} = \frac{\partial u_z}{\partial z},\ \varepsilon_{\varphi\varphi} = \frac{u_r}{r},\ \varepsilon_{\varphi z} = 0,\ \varepsilon_{r\varphi} = 0,\ \varepsilon_{rz} = 0 \tag{11}$$

Thus, the complete mathematical arrangement of the problem includes the balance Equation (6) with the boundary conditions (7), closing relations (8) and (9), and physical (1) and geometrical (11) relationships.

The disk deformation is determined by the rotational rate ω. If the latter is low, the disk deformation is elastic. When the rotational rate grows, the inner disk surface undergoes plastic deformation [84]. The plastic zone occupies the ring domain with an increasing rotational rate, i.e., $R_{\text{in}} \le r \le R_{\text{pl}}$. The outer ring remains in the elastic state, i.e., $R_{\text{pl}} < r \le R_{\text{ex}}$. Thus, we can identify four situations for the deformation process of the rotating disk:

1. The whole disk is in the elastic state ($\omega < \omega_{\text{el}}$).
2. The disk is in the elastic state, but its inner surface is in the plastic state ($\omega = \omega_{\text{el}}$).
3. Inner disk layers $r \le R_{\text{pl}}$ are in the plastic state, while outer layers $r > R_{\text{pl}}$ are in the elastic state ($\omega_{\text{el}} < \omega < \omega_{\text{pl}}$).
4. The disk material is in the plastic state throughout its width ($\omega = \omega_{\text{pl}}$).

Let us discuss the elastic deformation of the disk. In this case, stress and strain are both determined by Hooke's law. Since $\sigma_{zz} = 0$, the following relations result from Hooke's law:

$$\begin{gathered}\varepsilon_{rr} = \frac{1}{2G_{\text{eff}}(1+\nu)}\left(\sigma_{rr} - \nu\sigma_{\varphi\varphi}\right),\ \ \varepsilon_{\varphi\varphi} = \frac{1}{2G_{\text{eff}}(1+\nu)}\left(\sigma_{\varphi\varphi} - \nu\sigma_{rr}\right),\\ \varepsilon_{zz} = -\frac{\nu}{2G_{\text{eff}}(1+\nu)}\left(\sigma_{rr} + \sigma_{\varphi\varphi}\right),\end{gathered} \tag{12}$$

where ν is the Poisson ratio, $G_{\text{eff}} = \Gamma_{\text{eff}}^{1/n}\sigma_{0.2}^{(n-1)/n}$ is the effective shear modulus.

Tangential stresses can be derived from (6) and applied to (12). We then use the equation of strain compatibility (8). The resulting differential second-order equation, which describes the radial stress σ_{rr} is as follows:

$$\frac{1}{r}\frac{\partial}{\partial r}\left[r^3\frac{\partial\sigma_{rr}}{\partial r}\right] + (3+\nu)\rho\omega^2 r^2 = 0 \tag{13}$$

After integration of this equation with respect to the boundary conditions (7), we can determine the radial stress in the disk:

$$\sigma_{rr} = -\frac{(3+\nu)}{8}\rho\omega^2\left(r^2 - \left(R_{\text{in}}^2 + R_{\text{ex}}^2\right) + \frac{R_{\text{in}}^2 R_{\text{ex}}^2}{r^2}\right) \tag{14}$$

The tangential stress $\sigma_{\varphi\varphi}$ is derived from the balance equation (6):

$$\sigma_{\varphi\varphi} = r\frac{\partial\sigma_{rr}}{\partial r} + \sigma_{rr} + \rho\omega^2 r^2 \tag{15}$$

Substitution of (14) into (15) yields

$$\sigma_{\varphi\varphi} = -\frac{(3+\nu)}{8}\rho\omega^2\left(3r^2 - \left(R_{\text{in}}^2 + R_{\text{ex}}^2\right) - \frac{R_{\text{in}}^2 R_{\text{ex}}^2}{r^2}\right) + \rho\omega^2 r^2 \tag{16}$$

The stress in the disk grows with an increasing rotational rate. When the latter reaches a certain value ω_{el}, plastic deformation occurs on the inner disk surface. The rotational rate describes the elastic limit of the disk. In order to determine the rotational rate, at which plastic deformation occurs on the inner surface, we use the tangential stress from

(16) at $r = R_{in}$. Note that the strain intensity relating to the elastic-plastic transition is $\varepsilon_{pl} = \sigma_{0.2}/G_{eff}$. Thus, we obtain the following:

$$\omega_{el} = \sqrt{\frac{4\sigma_{0.2}}{\rho\left((3+\nu)R_{ex}^2 + (1-\nu)R_{in}^2\right)}} \tag{17}$$

Let us now determine the conditions of the elastic–plastic transition for the whole disk material. It occurs when the rotational rate is $\omega = \omega_{pl}$.

The analysis of plastic deformation is based on the Tresca–Saint Venant criterion. Since the radial σ_{rr} and tangential $\sigma_{\varphi\varphi}$ stresses are tensile, they are positive, viz. $\sigma_{rr} > 0$, $\sigma_{\varphi\varphi} > 0$. Moreover, we take into account that tangential stresses exceed radial ($\sigma_{\varphi\varphi} > \sigma_{rr}$). Due to the plane state, the axial stress σ_{zz} is absent ($\sigma_{zz} = 0$). Hence, the conditions of the material hardening (9) and fracture (10) are calculated as follows:

$$\sigma_{\varphi\varphi} = \Gamma_{eff}\varepsilon^n, \;\; \sigma_{\varphi\varphi} \geq \sigma_B \tag{18}$$

According to multiple experiments, the volume does not change during plastic deformation, and the following condition is satisfied:

$$\varepsilon_V = \varepsilon_{rr} + \varepsilon_{\varphi\varphi} + \varepsilon_{zz} = 0 \tag{19}$$

Taking the plane problem and (10) and (19) into consideration, it can be concluded that the axial strain ε_{zz} does not depend on the coordinate z and can be either the function of radial coordinate r or a constant. The absence of the shear stress ($\sigma_{rz} = 0$) implies that the axial strain is a constant value.

Using (11), the condition of incompressibility ($\varepsilon_V = 0$) is written as follows:

$$\frac{\partial u_r}{\partial r} + \frac{u_r}{r} + \varepsilon_{zz} = 0 \tag{20}$$

The integration of (20) within the accuracy of integration constants allows us to determine the displacement field:

$$u_r = -\varepsilon_{zz}\frac{r}{2} + \frac{C_1}{r} \tag{21}$$

Considering Cauchy relations (11), the radial and tangential strains are written as follows:

$$\varepsilon_{rr} = -\frac{\varepsilon_{zz}}{2} - \frac{C_1}{r^2}; \; \varepsilon_{\varphi\varphi} = -\frac{\varepsilon_{zz}}{2} + \frac{C_1}{r^2} \tag{22}$$

In solid mechanics, an invariant variable is introduced to describe the deformation field called the shear strain intensity, which, according to Il'yushin [84,85], is determined by the following expression:

$$\varepsilon = \sqrt{\frac{2}{3}}\sqrt{\left(\varepsilon_{rr} - \varepsilon_{\varphi\varphi}\right)^2 + \left(\varepsilon_{zz} - \varepsilon_{\varphi\varphi}\right)^2 + \left(\varepsilon_{rr} - \varepsilon_{zz}\right)^2} \tag{23}$$

Substituting (22) into (23), we obtain the dependence between the shear strain intensity and radial coordinate:

$$\varepsilon = \sqrt{4\left(\frac{C_1}{r^2}\right)^2 + 3\varepsilon_{zz}^2} \tag{24}$$

In order to derive the axial strain ε_{zz}, let us use (12). It follows that the axial strain is as follows:

$$\varepsilon_{zz} = -\frac{\nu}{2G_{eff}(1+\nu)}\left(\sigma_{rr} + \sigma_{\varphi\varphi}\right) = -\frac{\nu}{2G_{eff}(1+\nu)}\sigma_{0.2} \tag{25}$$

Since the axial strain ε_{zz} is constant, (25) holds for the whole disk. Considering the plastic state of the whole disk, the radial stress on its outer boundary equals the yield strength:

$$r = R_{\text{ex}}: \ \sigma_{\varphi\varphi} = \sigma_{0.2} \tag{26}$$

Now we can derive the integration constant C_1 according to (24) and (26):

$$C_1 = \frac{R_{\text{ex}}^2}{2}\sqrt{\left(\frac{\sigma_{0.2}}{G_{\text{eff}}}\right)^2 - 3\varepsilon_{zz}^2} = \frac{R_{\text{ex}}^2}{4(1+\nu)}\frac{\sigma_{0.2}}{G_{\text{eff}}}\sqrt{4+8\nu+\nu^2} \tag{27}$$

Let us consider the nonlinear hardening described by (18) to calculate the stress–strain state of the disk and the rotational rate limit at which the plastic zone covers the whole disk.

Using (18), (22), (24), we can find the tangential stress $\sigma_{\varphi\varphi}$ for the case of nonlinear hardening:

$$\sigma_{\varphi\varphi} = \sigma_{0.2}\left(\frac{\sqrt{3}}{2}\frac{\nu}{(1+\nu)}\right)^n\left(\frac{4+8\nu+\nu^2}{3\nu^2}\frac{R_{\text{ex}}^4}{r^4}+1\right)^{n/2} \tag{28}$$

To simplify further integration, we write (28) in the form as follows:

$$\sigma_{\varphi\varphi} = \sigma_*\left(\frac{R_*^4}{r^4}+1\right)^{n/2} \tag{29}$$

where $\sigma_* = \sigma_{0.2}\left(\frac{\sqrt{3}}{2}\frac{\nu}{(1+\nu)}\right)^n$ and $R_* = \left(\frac{4+8\nu+\nu^2}{3\nu^2}\right)^{1/4}R_{\text{ex}}$.

The radial stress σ_{rr} is derived from the balance Equation (6), which can be written as the following relation with regard to the nonlinear dependence between hardening and deformation:

$$\frac{\partial r\sigma_{rr}}{\partial r} = \sigma_*\left(\frac{R_*^4}{r^4}+1\right)^{n/2} - \rho\omega^2 r^2 \tag{30}$$

The integration of (30) results in the σ_{rr} dependence on the radial coordinate r:

$$\sigma_{rr} = \frac{\sigma_*}{1-2n}\cdot\left(\frac{R_*}{r}\right)^{2n}{}_2F_1\left(\frac{1}{4}-\frac{n}{2},-\frac{n}{2};\frac{5}{4}-\frac{n}{2};-\frac{r^4}{R_*^4}\right) - \frac{1}{3}\rho\omega^2 r^2 + C_2\frac{R_{\text{ex}}}{r} \tag{31}$$

In (31), C_2 is the integration constant and ${}_2F_1$ is the hypergeometric Gaussian function determined by the Gaussian series sum:

$${}_2F_1(a,b;c;z) = 1 + \sum_{k=1}^{\infty}\left[\prod_{l=0}^{k-1}\frac{(a+l)(b+l)}{(1+l)(c+l)}\right]z^k \tag{32}$$

At the disk boundary ($r = R_{\text{out}}$), radial stresses are assumed to be absent ($\sigma_{rr} = 0$). Hence, the integration constant C_2 is as follows:

$$C_2 = \frac{1}{3}\rho\omega^2 R_{\text{ex}}^2 - \frac{\sigma_*}{1-2n}\cdot\left(\frac{R_*}{R_{\text{ex}}}\right)^{2n}{}_2F_1\left(\frac{1}{4}-\frac{n}{2},-\frac{n}{2};\frac{5}{4}-\frac{n}{2};-\frac{R_{ex}^4}{R_*^4}\right) \tag{33}$$

The rotational rate of the disk, at which its material transfers to the plastic state ($\omega = \omega_{\text{pl}}$), is obtained from the condition of the inner disk boundary, viz. $r = R_{\text{in}}$, $\sigma_{rr} = 0$:

$$\omega_{\text{pl}} = \sqrt{\frac{3\sigma_*}{\rho(1-2n)}\frac{R_{\text{in}}}{R_{\text{in}}^3 - R_{\text{ex}}^3}\cdot\left[\left(\frac{R_*}{R_{\text{in}}}\right)^{2n}{}_2F_1\left(\frac{1}{4}-\frac{n}{2},-\frac{n}{2};\frac{5}{4}-\frac{n}{2};-\frac{R_{\text{in}}^4}{R_*^4}\right) - \frac{R_{\text{ex}}}{R_{\text{in}}}\left(\frac{R_*}{R_{\text{ex}}}\right)^{2n}{}_2F_1\left(\frac{1}{4}-\frac{n}{2},-\frac{n}{2};\frac{5}{4}-\frac{n}{2};-\frac{R_{ex}^4}{R_*^4}\right)\right]} \tag{34}$$

4. Mathematical Simulation

Plastic strain in the disk is conditioned by the centrifugal force field. The impact of these forces is evaluated by the resulting centrifugal bulk force:

$$f^* = \frac{2}{3}\rho\omega^2 \frac{R_{ex}^2 + R_{ex}R_{in} + R_{in}^2}{R_{ex} + R_{in}} \quad (35)$$

Thus, the centrifugal force increases with increasing outer radius R_{ex} at the constant inner radius R_{in}, i.e., $h = R_{ex} - R_{in}$, and increasing inner radius at a constant outer radius, i.e., with decreasing disk width h.

Figure 4 presents plots of the rotational rate at which plastic strain ω_{el} begins and the disk width $h = R_{ex} - R_{in}$. As can be seen in Figure 4, the circular disk resistance to plastic strain depends on the R_{in}/R_{ex} ratio. When the disk width expands at the constant R_{in}, the resistance reduces due to the increase in the centrifugal force field. On the contrary, when the disk width expands at the constant R_{ex}, the centrifugal force reduces and the plastic transfer occurs at a higher rotation frequency. Note that the width effect on the plastic strain ω_{el} is more significant for a small R_{in}/R_{ex} ratio. The plastic strain slightly increases with the increasing R_{in}/R_{ex} ratio. When the inner and outer radii increase at the same disk width, the centrifugal force applied to the disk increases. This results in a reduction in the plastic resistance, which occurs at a lower plastic strain.

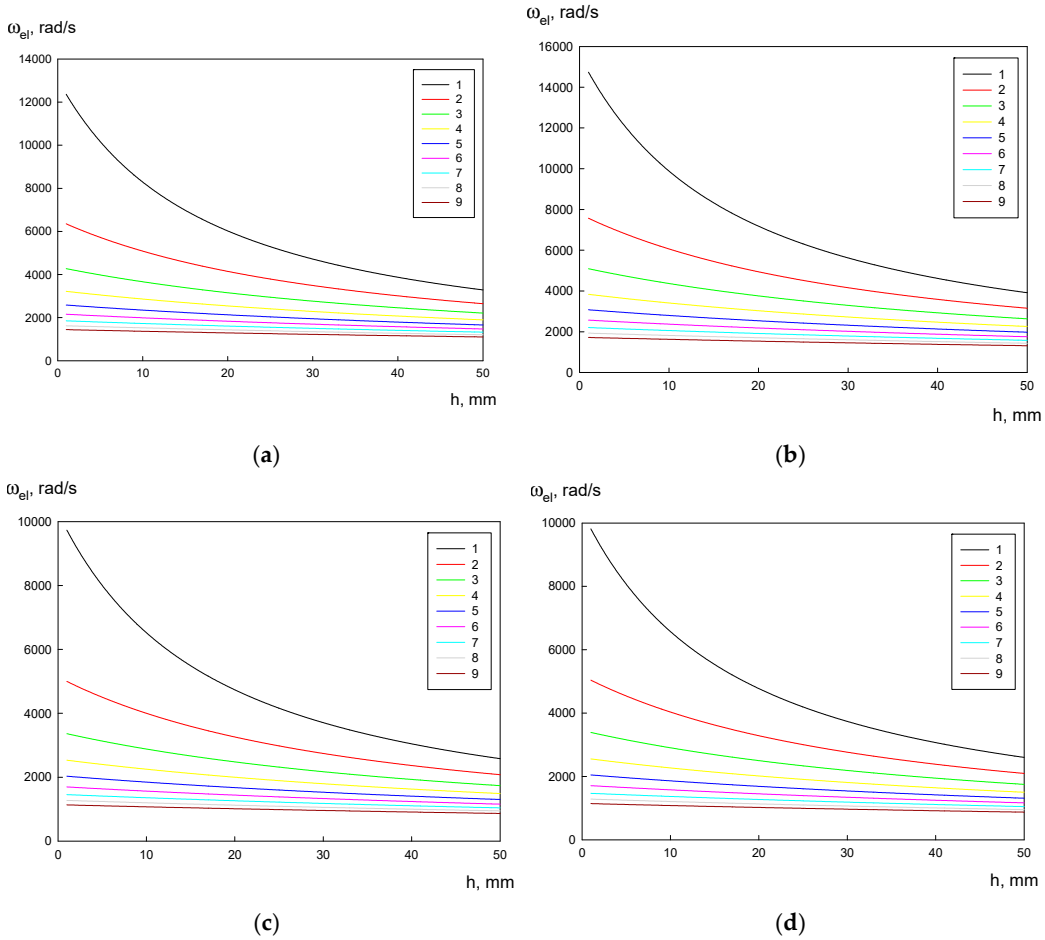

Figure 4. Dependences of disk width and rotational rate, at which plastic strain ω_{el} begins in different alloys and different R_{in}: (**a**) A356; (**b**) A356–0.5TiB_2; (**c**) AA5056; (**d**) AA5056–Al_3Er; 1—15 mm, 2—30 mm, 3—45 mm, 4—60 mm, 5—75 mm, 6—90 mm, 7—105 mm, 8—120 mm, and 9—135 mm.

The plastic strain of the inner radius is also affected by the conventional yield strength $\sigma_{0\cdot2}$. Due to its growth, the plastic resistance increases, which requires a more intensive

disk rotation. Thus, the plastic strain ω_{el} becomes the highest for the A356–0.5%TiB_2 alloy, whereas, for the AA5056 alloy, it is the lowest.

In Figure 5, one can see plots of the radial stress and coordinate. Since the outer and inner radii are not subjected to radial loads, at $r = R_{ex}$ and $r = R_{in}$, the radial stress is zero, viz. $\sigma_{rr} = 0$. The maximum radial stress σ_{rr}^m occurs at the $R_m = \sqrt{R_{in}R_{ex}}$ point, which is the geometric average of the inner and outer radii. The radial stress increases with an increasing disk width and rotational rate:

$$\sigma_{rr}^m = \frac{(3+\nu)}{8}\rho\omega^2 h^2 \tag{36}$$

As mentioned above, the plastic state occurs on the inner disk surface at $\omega = \omega_{el}$. In this case, the maximum radial stress is calculated as follows:

$$\sigma_{rr}^m = \frac{(3+\nu)}{2}\sigma_{0.2}\frac{(R_{ex}-R_{in})^2}{(3+\nu)R_{ex}^2+(1-\nu)R_{in}^2} \tag{37}$$

Equation (36) can be written as the following:

$$\sigma_{rr}^m = \frac{(3+\nu)}{2}\sigma_{0.2}\frac{1-2\xi+\xi^2}{(3+\nu)+(1-\nu)\xi^2} \tag{38}$$

where $\xi = R_{in}/R_{ex}$ is the ratio between the inner and outer radii. The maximum radial stress σ_{rr}^m monotonically decreases with increasing ξ. In the case of the solid disk ($\xi = 0$), this stress is 50% of the conventional yield strength, viz. $\sigma_{rr}^m = 0.5\sigma_{0.2}$.

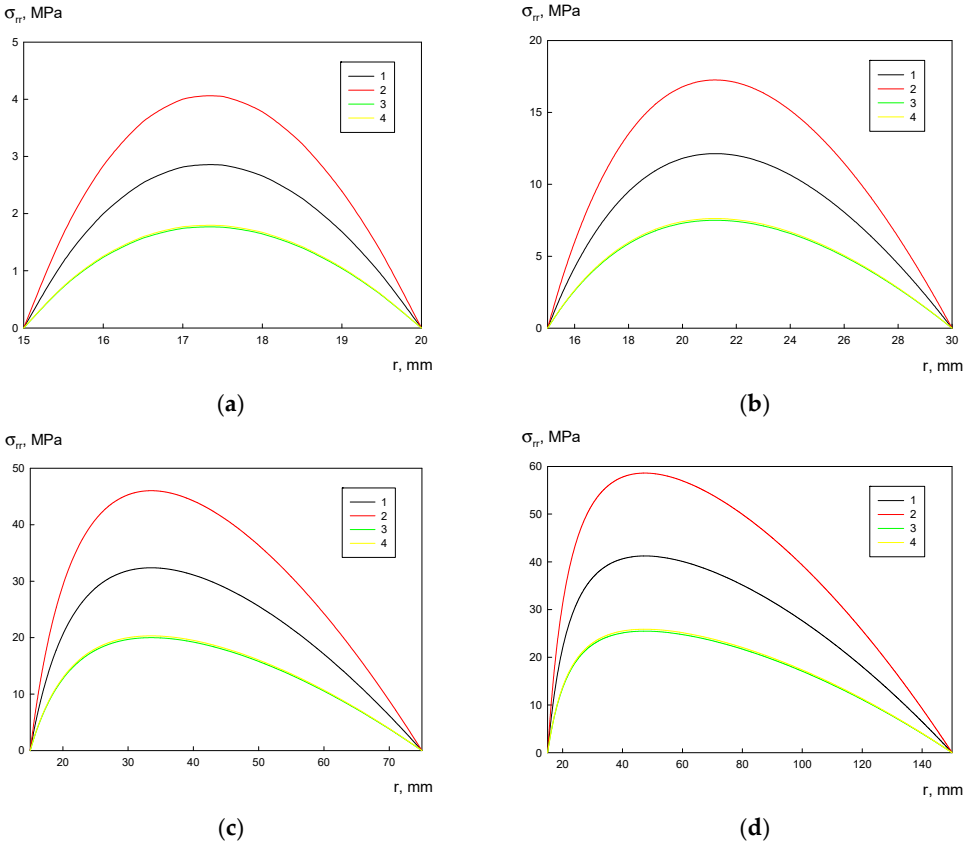

Figure 5. *Cont.*

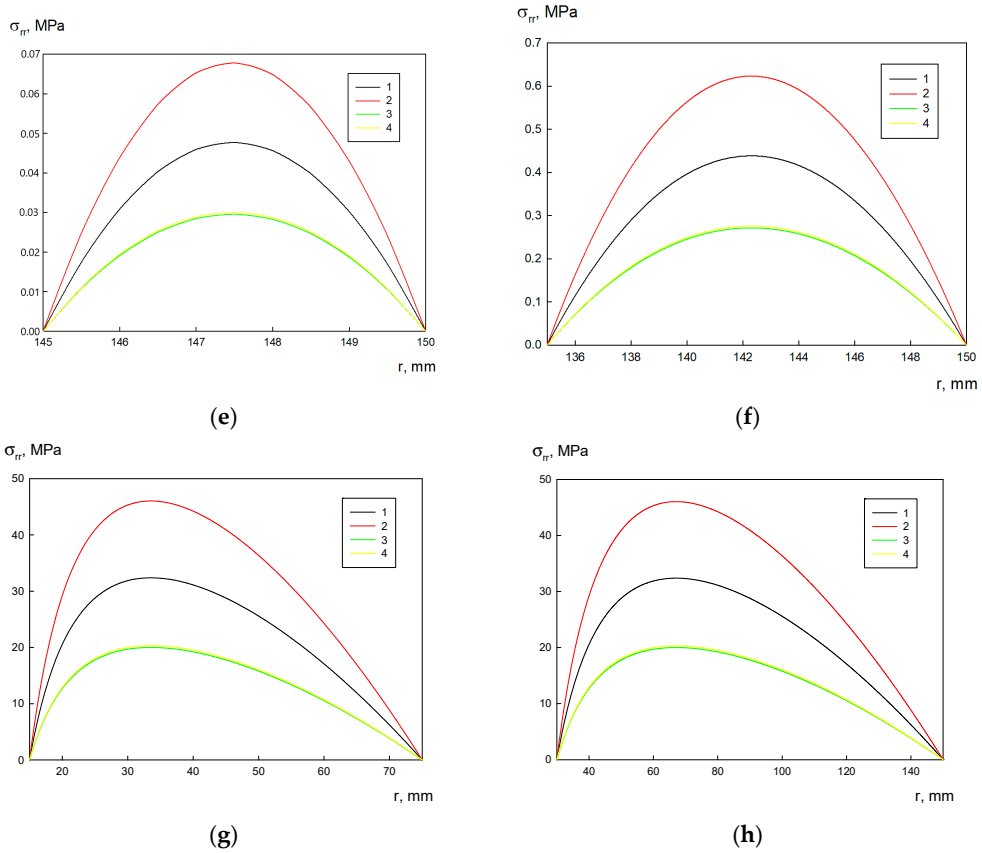

Figure 5. Stress σ_{rr} distribution over the disk radii: (**a**) $R_{\text{in}} = 15$ mm, $R_{\text{ex}} = 20$ mm; (**b**) $R_{\text{in}} = 15$ mm, $R_{\text{ex}} = 30$ mm; (**c**) $R_{\text{in}} = 15$ mm, $R_{\text{ex}} = 75$ mm; (**d**) $R_{\text{in}} = 15$ mm, $R_{\text{ex}} = 150$ mm; (**e**) $R_{\text{in}} = 145$ mm, $R_{\text{ex}} = 150$ mm; (**f**) $R_{\text{in}} = 135$ mm, $R_{\text{ex}} = 150$ mm; (**g**) $R_{\text{in}} = 75$ mm, $R_{\text{ex}} = 150$ mm; (**h**) $R_{\text{in}} = 30$ mm, $R_{\text{ex}} = 150$ mm; 1—A356, 2—A356–0.5 TiB_2, 3—AA5056, and 4—AA5056–Al_3Er.

The radial distribution of tangential stress $\sigma_{\varphi\varphi}$ is presented in Figure 6. The tangential stress $\sigma_{\varphi\varphi}$ is the highest on the inner disk radius and is calculated as follows:

$$\sigma_{\varphi\varphi}(R_{\text{in}}) = \frac{\rho\omega^2}{4}\left[(1-\nu)R_{\text{in}}^2 + (3+\nu)R_{\text{ex}}^2\right] \tag{39}$$

The tangential stress monotonically decreases with the increasing radial coordinate r and its lowest value is observed at the outer disk radius:

$$\sigma_{\varphi\varphi}(R_{\text{ex}}) = \frac{\rho\omega^2}{4}\left[(1-\nu)R_{\text{ex}}^2 + (3+\nu)R_{\text{in}}^2\right] \tag{40}$$

Nonuniform tangential stress distribution in the disk material describes the ratio between the stresses on the outer and inner disk boundaries. This ratio θ is obtained from the following:

$$\theta = \frac{\sigma_{\varphi\varphi}(R_{\text{ex}})}{\sigma_{\varphi\varphi}(R_{\text{in}})} = \frac{(1-\nu)+(3+\nu)\xi^2}{(1-\nu)\xi^2+(3+\nu)} \tag{41}$$

It is interesting to note that the ratio θ does not depend on the material and the rotational rate, and is rather determined by the disk geometry. At $\xi = 0$ (solid disk), this ratio is the lowest, i.e., $\theta = (1-\nu)/(3+\nu)$, whereas at a higher ξ, $\theta \to 1$.

When the inner disk surface is in the plastic state, which occurs at $\omega = \omega_{\text{el}}$, the tangential stresses at the disk boundaries are as follows:

$$\sigma_{\varphi\varphi}(R_{\text{in}}) = \sigma_{0.2}, \;\; \sigma_{\varphi\varphi}(R_{\text{ex}}) = \frac{(1-\nu)+(3+\nu)\xi^2}{(3+\nu)+(1-\nu)\xi^2}\sigma_{0.2} \tag{42}$$

Now we consider the case when the rotational rate is $\omega = \omega_{pl}$ and the whole disk is in the plastic state. The lowest tangential stress $\sigma_{\varphi\varphi}$ appears on the outer disk boundary ($r = R_{ex}$) and equals $\sigma_{0.2}$. The highest tangential stress is observed on the inner disk boundary ($r = R_{in}$) and is obtained from the following:

$$\sigma_{\varphi\varphi}(R_{in}) = \sigma_* \left(\frac{R_*^4}{R_{in}^4} + 1 \right)^{n/2} = \sigma_{0.2} \left(\frac{(4 + 8\nu + \nu^2)\xi^{-4} + 3\nu^2}{4(1+\nu)^2} \right)^{n/2} \quad (43)$$

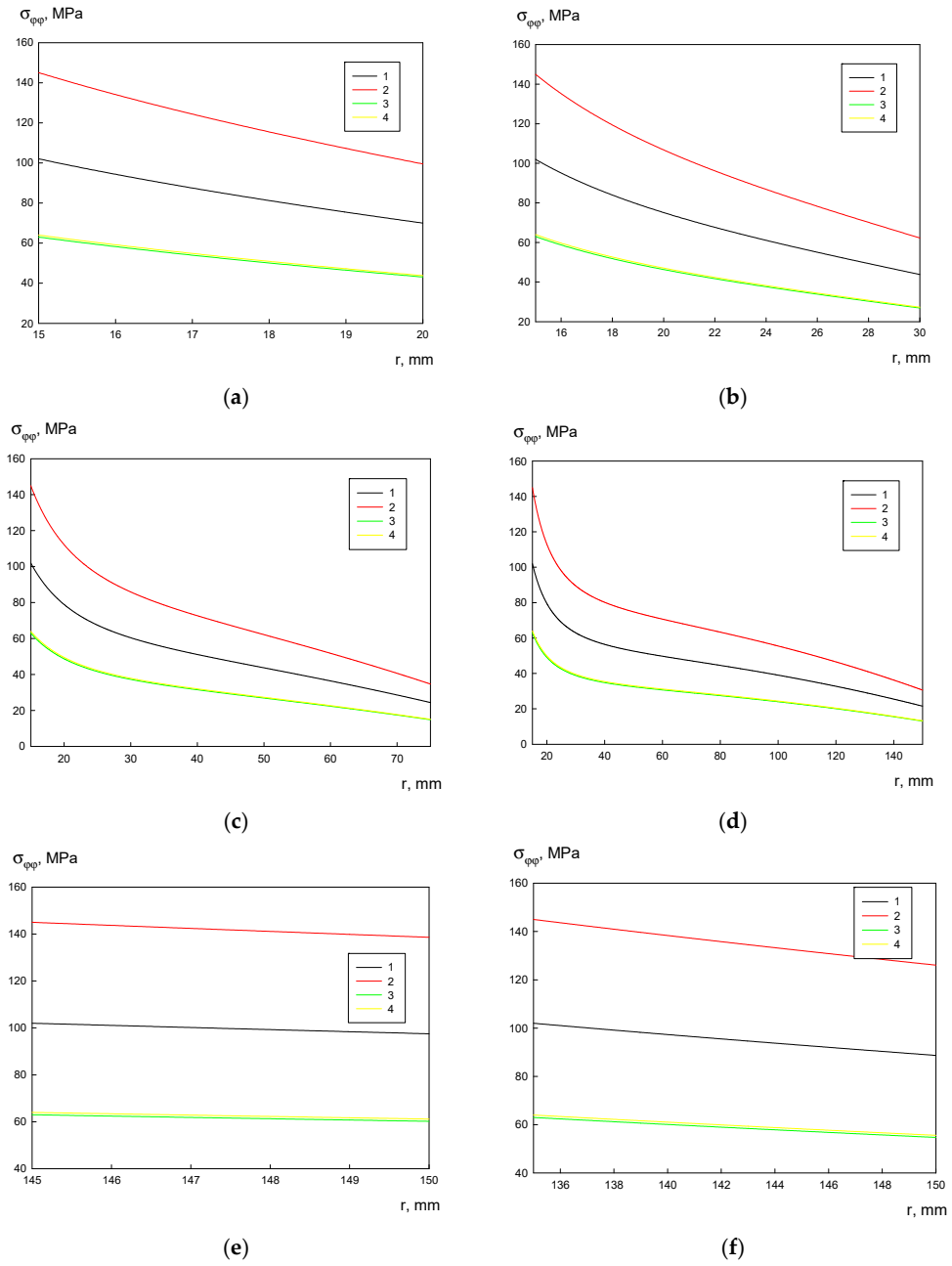

Figure 6. *Cont.*

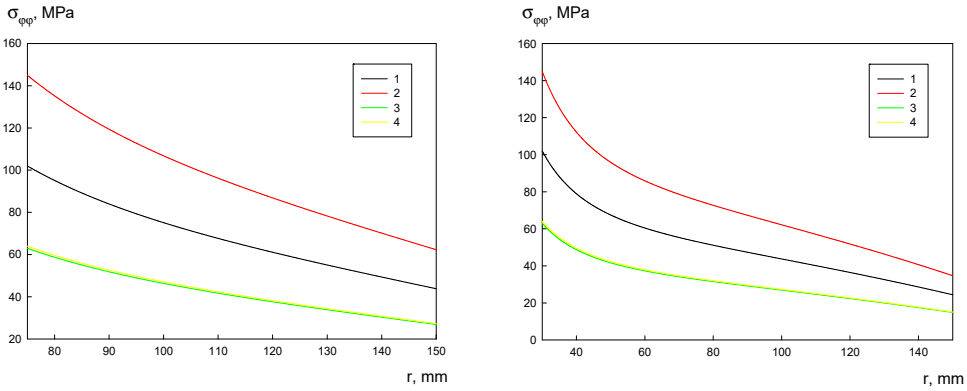

(**g**) (**h**)

Figure 6. Stress $\sigma_{\varphi\varphi}$ distribution over the disk radii: (**a**) $R_{\text{in}} = 15$ mm, $R_{\text{ex}} = 20$ mm; (**b**) $R_{\text{in}} = 15$ mm, $R_{\text{ex}} = 30$ mm; (**c**) $R_{\text{in}} = 15$ mm, $R_{\text{ex}} = 75$ mm; (**d**) $R_{\text{in}} = 15$ mm, $R_{\text{ex}} = 150$ mm; (**e**) $R_{\text{in}} = 145$ mm, $R_{\text{ex}} = 150$ mm; (**f**) $R_{\text{in}} = 135$ mm, $R_{\text{ex}} = 150$ mm; (**g**) $R_{\text{in}} = 75$ mm, $R_{\text{ex}} = 150$ mm; (**h**) $R_{\text{in}} = 30$ mm, $R_{\text{ex}} = 150$ mm; 1—A356, 2—A356–0.5 TiB_2, 3—AA5056, and 4—AA5056–Al_3Er.

It follows from (43) that at low ξ values, tangential stresses are higher and can exceed the USL σ_B. At the disk rotational rate $\omega = \omega_{\text{pl}}$ and with respect to (18) and (43), the condition of the disk strength retention can be defined as follows:

$$\sigma_B > \sigma_{\varphi\varphi}(R_{\text{in}}) \tag{44}$$

Equations (43) and (44) help to determine the geometrical parameter ξ, at which the disk fracture does not occur:

$$\xi_B = \left(\frac{(4 + 8\nu + \nu^2)}{4(1+\nu)^2 \left(\frac{\sigma_B}{\sigma_{0.2}}\right)^{2/n} - 3\nu^2} \right)^{1/4} < \xi \tag{45}$$

The ξ_B parameter values characterizing the disk strength at $\omega = \omega_{\text{pl}}$ are given in Table 3.

Table 3. Parameter ξ_B values (45).

Alloys	ξ_B
A356	0.508
A356–0.5TiB_2	0.631
AA5056	0.229
AA5056–Al_3Er	0.143

Note that the disk fracture may occur at $\omega < \omega_{\text{pl}}$, when the inner and outer disk boundaries are deformed plastically and elastically, respectively. The analysis of this case falls outside the scope of this work and will be addressed in our future works.

In Figure 7, the dependences of the limit frequency ω_{pl} of rotation and the width h show the plastic zone, which occupies the whole disk with different radii R_{in}. At the constant value of the inner radius R_{in}, the centrifugal forces increase with an increasing width h. Therefore, the plastic strain of the disk occurs at a lower limit frequency ω_{pl}. The plastic resistance increases with the decreasing inner radius R_{in}, and total plastic deformation of the disk occurs at higher values of the limit frequency ω_{pl}. In wide annular disks ($R_{\text{in}}(1/\xi_B - 1) < h$), the strength loss occurs at the inner disk boundary at $\omega = \omega_{\text{pl}}$, and the disk fracture begins. In Figure 7, one can see two zones for different geometrical parameters: A denotes no fracture, and B denotes a fracture at the inner disk boundary.

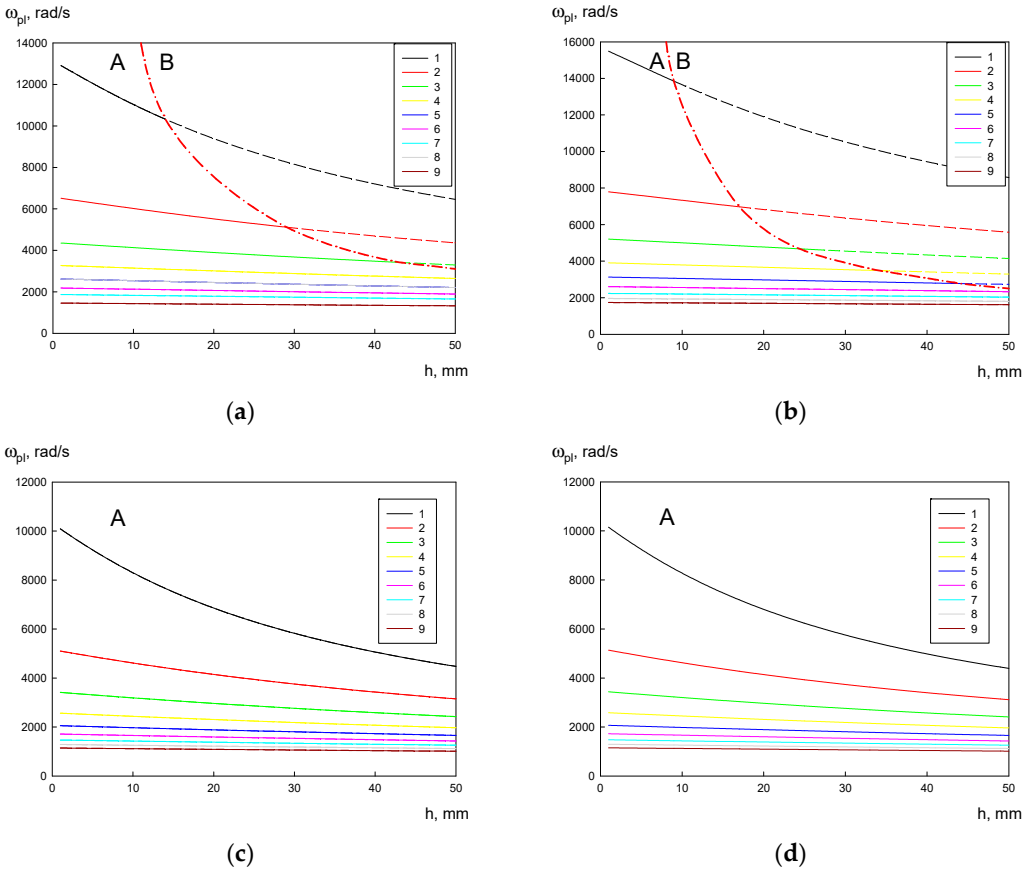

Figure 7. Dependences between the limit frequency ω_{pl} of the rotation and disk width when the plastic zone occupies the whole disk made of different alloys: (**a**) A356; (**b**) A356–0.5TiB_2; (**c**) AA5056; (**d**) AA5056–Al_3Er; 1—R_{in} = 15 mm, 2—R_{in} = 30 mm, 3—R_{in} = 45 mm, 4—R_{in} = 60 mm, 5—R_{in} = 75 mm, 6—R_{in} = 90 mm, 7—R_{in} = 105 mm, 8—R_{in} = 120 mm, and 9—R_{in} = 135 mm. A—no fracture, B—fracture on the inner disk boundary.

The parameter $\delta = \left(\omega_{\text{pl}} - \omega_{\text{el}}\right)/\omega_{\text{el}}$ can be used to describe the disk plastic properties. At low δ values, a slight increase in the rotational rate leads to the expansion of the plastic zone from the inner to the outer disk boundary. At a high δ parameter, the limit frequency ω_{pl} must be significantly higher than the plastic strain ω_{el} to gain total plastic deformation.

Figure 8 illustrates δ and width h dependence plots when the plastic zone occupies the whole disk with different inner radius R_{in}. In the narrow disks ($h \leq 5$ mm), the parameter δ contributes only a few percent. At the increased width h and fixed R_{in}, the δ parameter increases. This means that there is a wide range of rotational rates, which determines the transition of plastic strain on the inner boundary to the plastic strain of the whole disk. At a higher inner radius and constant width, the δ parameter decreases.

The distribution of the radial σ_{rr} and tangential $\sigma_{\varphi\varphi}$ stresses is presented in Figures 9 and 10. These curves are similar to those given in Figures 4 and 5. The radial stress σ_{rr} is characterized by the maximum, which increases with increasing R_{in}/R_{ex} ratio. In our case, this stress is zero on the outer and inner radii as they are not loaded with radial forces.

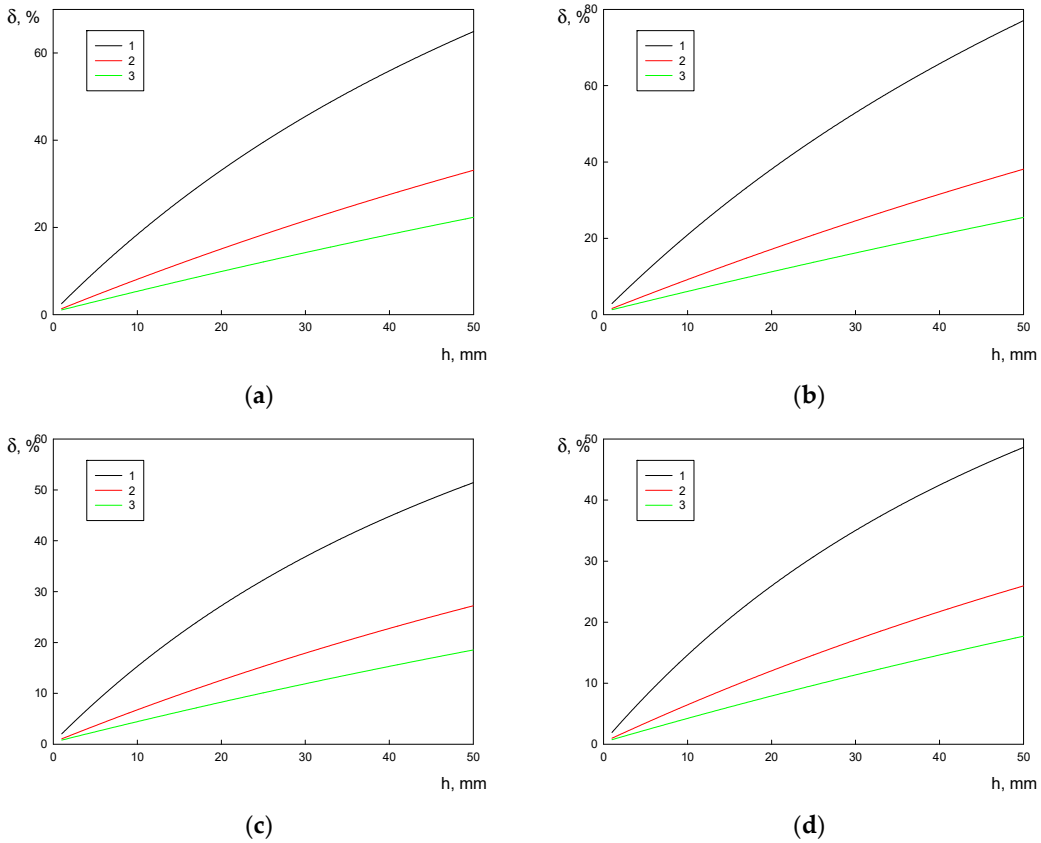

Figure 8. Parameter δ/width dependence for different alloys and radii: (**a**) A356; (**b**) A356–0.5TiB_2; (**c**) AA5056; (**d**) AA5056–Al_3Er; 1—R_{in} = 30 mm, 2—R_{in} = 60 mm, and 3—R_{in} = 105 mm.

The tangential stress $\sigma_{\varphi\varphi}$ monotonically decreases with increasing radial coordinate r. The lowest tangential stress is observed on the outer disk boundary ($r = R_{ex}$). At $\omega = \omega_{pl}$, the tangential stress on the outer disk boundary equals the yield strength. When approaching the inner diameter, the tangential stress increases. It is worth noting that at the disk geometrical parameters in Figures 8 and 9, its fracture does not occur. Additionally, with increasing R_{in}/R_{ex} ratio, the tangential stress decreases.

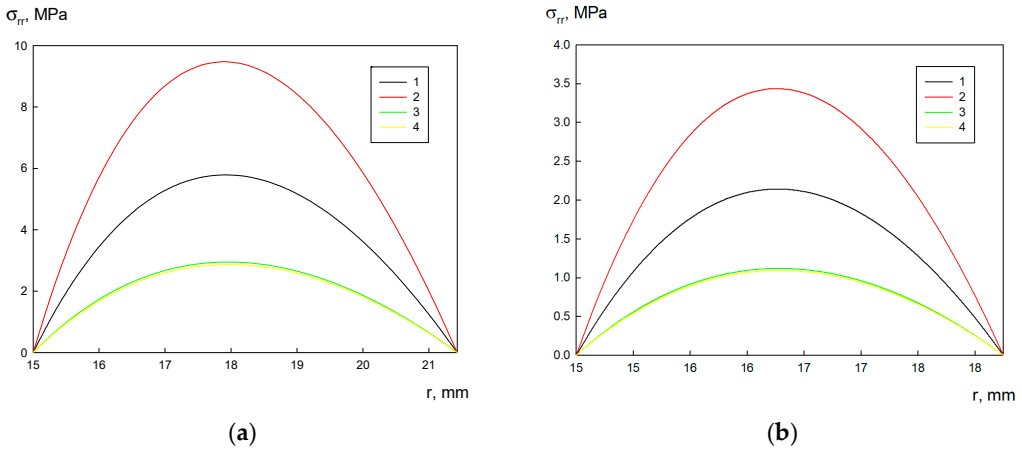

Figure 9. *Cont.*

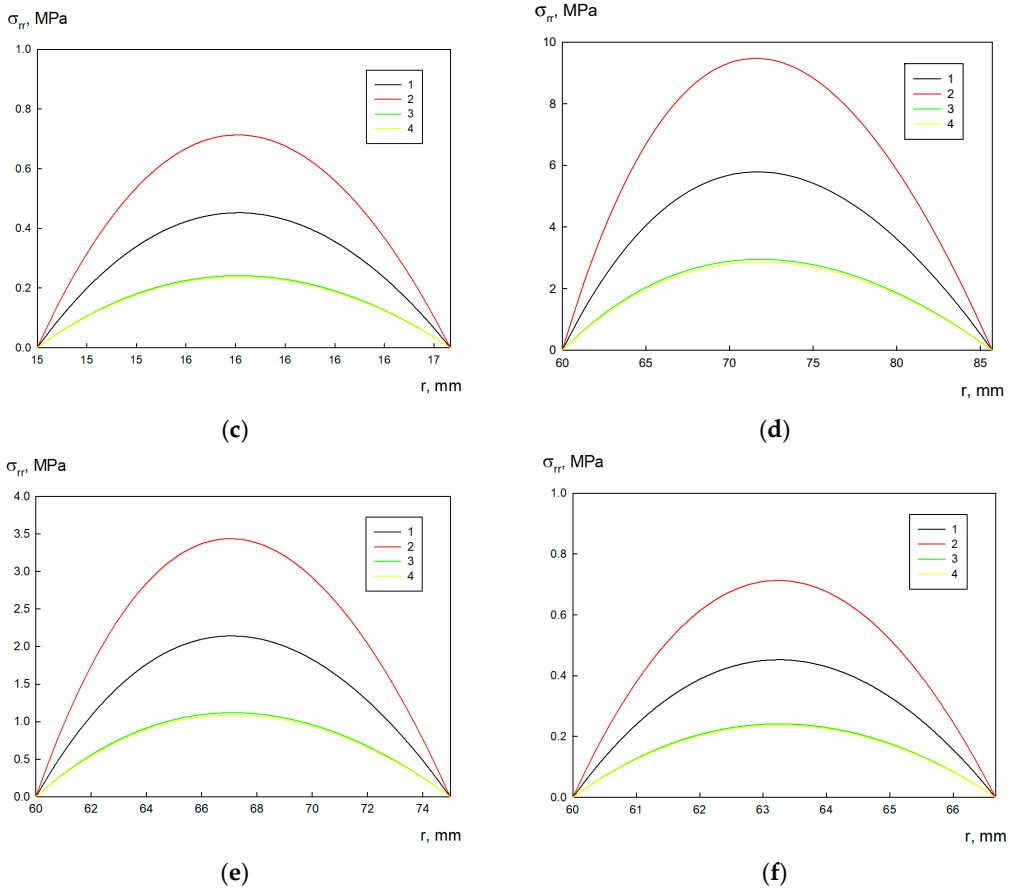

Figure 9. Stress σ_{rr} distribution over the disk radii: (**a**) R_{in} = 15 mm, ξ = 0.7; (**b**) R_{in} = 15 mm, ξ = 0.8; (**c**) R_{in} = 15 mm, ξ = 0.9; (**d**) R_{in} = 60 mm, ξ = 0.7; (**e**) R_{in} = 60 mm, ξ = 0.8; (**f**) R_{in} = 60 mm, ξ = 0.9; 1—A356, 2—A356–0.5TiB_2, 3—AA5056, and 4—AA5056–Al_3Er.

The inner radius R_{in} values do not affect the distribution of radial σ_{rr} and tangential $\sigma_{\varphi\varphi}$ stresses in the disk material. The stress distribution over the disk width $\eta = r - R_{in}$ calculated for different inner radii is identical.

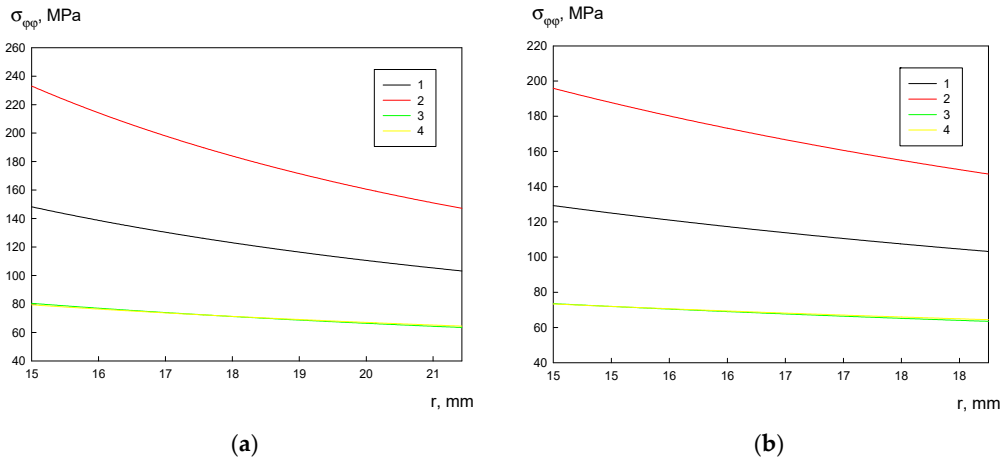

Figure 10. *Cont.*

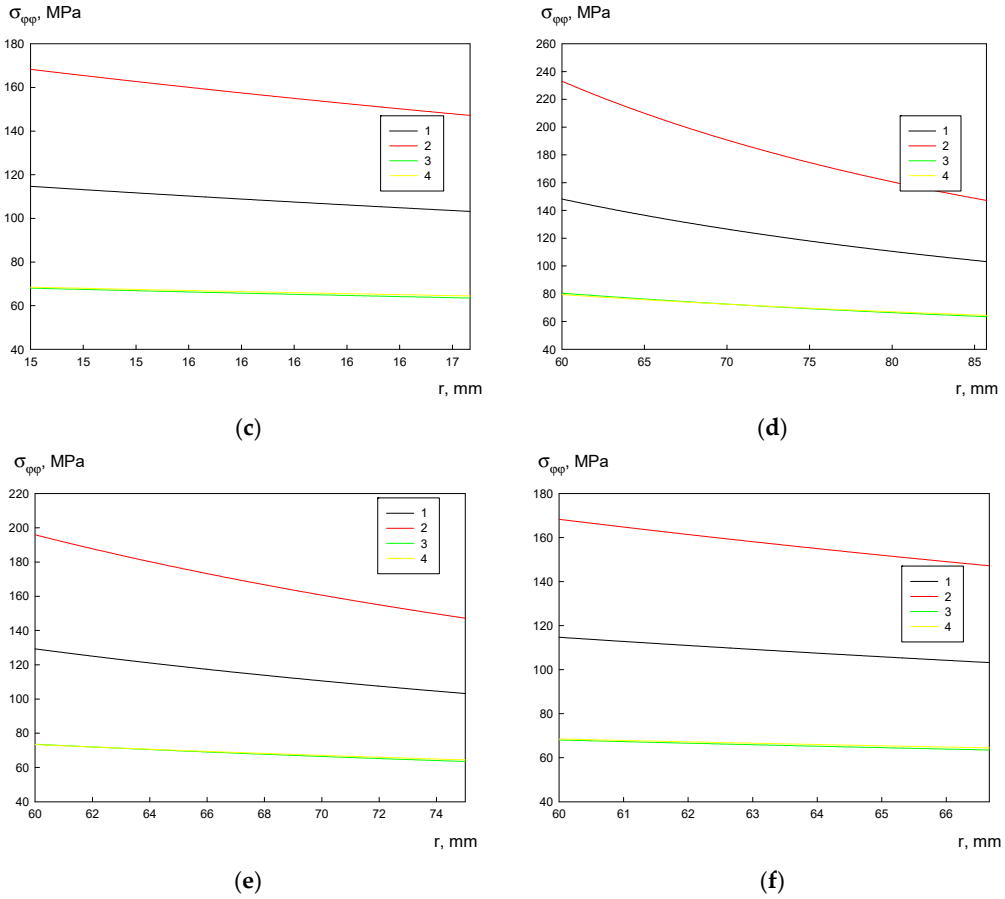

Figure 10. Stress σ_{rr} distribution over the disk radii: (**a**) R_{in} = 15 mm, ξ = 0.7; (**b**) R_{in} = 15 mm, ξ = 0.8; (**c**) R_{in} = 15 mm, ξ = 0.9; (**d**) R_{in} = 60 mm, ξ = 0.7; (**e**) R_{in} = 60 mm, ξ = 0.8; (**f**) R_{in} = 60 mm, ξ = 0.9; 1—A356, 2—A356–0.5TiB_2, 3—AA5056, and 4—AA5056–Al_3Er.

5. Conclusions

This paper investigated the stress–strain state, elastoplastic deformation, and disintegration conditions of the rotating circular disk made of the aluminum alloy strengthened with dispersed nanoparticles.

Aluminum alloys AA5056 and A356 with the use of master alloys AA5056–Al_3Er and A356–TiB_2 were employed as initial materials. According to tensile strength testing of the obtained alloys, the diffusion of Al_3Er particles improved the USL and plasticity of the AA5056 alloy from 170 to 204 MPa and from 14.7 to 21%, respectively, although a modifying effect was not observed during crystallization. The addition of TiB_2 particles to the A356 alloy composition also led to a simultaneous increase in its yield strength, USL, and plasticity from 102 to 145 MPa, from 204 to 263 MPa, and from 2.3 to 2.8%, respectively.

The annular disk's ability to resist plastic depended on the ratio between its outer and inner radii. This plastic resistance decreased with increasing disk width at a constant inner radius, which was associated with a stronger effect from the centrifugal force field. On the contrary, when the disk width expanded at the constant R_{ex}, the centrifugal force was reduced, and the plastic transfer occurred at a higher rotation frequency.

The radial stresses on the outer and inner disk radii were zero since the radii were not loaded with radial forces. The maximum radial stress σ_{rr}^{m} was observed at the point inside the disk. The maximum radial stress increased with increasing Rin/Rex ratio and with increasing disk width and rotational rate. The tangential stress $\sigma_{\varphi\varphi}$ monotonically decreased with increasing radial coordinate r. The lowest tangential stress was achieved at the outer disk boundary ($r = R_{ex}$), whereas the highest tangential stresses were observed at the inner disk boundary ($r = R_{in}$).

At $\omega = \omega_{pl}$ and low values of $\xi = R_{in}/R_{ex}$, the tangential stresses were high and could exceed the USL. The critical disk widths were $0.97R_{in}$ and $0.58R_{in}$ for A356 and A356–0.5TiB_2 alloys, respectively. Additionally, for AA5056 and AA5056–Al_3Er alloys, the values were $3.37R_{in}$ and $5.99R_{in}$, respectively. Thus, A356 and A356–0.5TiB_2 alloys were more brittle than AA5056 and AA5056–Al_3Er alloys. It was found that at $h < R_{in}(1/\xi_B - 1)$, the alloy sequence was A356–0.5TiB_2, A356, AA5056, and AA5056–Al_3Er for the disks to withstand the highest rotational rate without fracture. For wide disks ($R_{in}(1/\xi_B - 1) < h$), AA5056 and AA5056–Al_3Er alloys were preferable for fabrication.

Author Contributions: Conceptualization, O.M. and I.Z.; methodology, O.D.; software, O.M.; validation, O.D., O.M. and V.P.; formal analysis, V.P.; investigation, I.Z.; resources, A.V.; data curation, A.V.; writing—original draft preparation, O.D.; writing—review and editing, V.V.; visualization, V.V.; supervision, V.V.; project administration, A.V.; funding acquisition, I.Z. All authors have read and agreed to the published version of the manuscript.

Funding: This work was carried out with financial support from the Ministry of Education and Science of the Russian Federation (State assignment No. FSWM-2020-0028).

Institutional Review Board Statement: Not applicable.

Informed Consent Statement: Not applicable.

Data Availability Statement: Not applicable.

Acknowledgments: The analyses were carried out with the equipment of the Tomsk Regional Core Shared Research Facilities Center of National Research Tomsk State University. The Center was supported by the Ministry of Science and Higher Education of the Russian Federation Grant No. 075-15-2021-693 (No. 13.RFC.21.0012).

Conflicts of Interest: The authors declare no conflict of interest.

References

1. Matthews, F.L.; Rawlings, R.D. *Composite Materials: Engineering and Science*; CRC Press: Boca Raton, FL, USA, 1999; p. 480.
2. Arnhold, V.; Hummert, K. *New Materials by Mechanical Alloying Techniques*; DGM Informationsgeselischaft Verlag: Oberursel, Germany, 1989; p. 269.
3. Weber, J.H.; Schelleng, R.D. *Dispersion-Strengthened Aluminum Alloys*; Marcel Dekker, Inc.: New York, NY, USA; Basel, Switzerland; Hong Kong, China, 1988; Part 1, Chapter 11, pp. 269–293.
4. El-Labban, H.F.; Abdelaziz, M.; Mahmoud, E.R. Modification of carbon steel by laser surface melting: Part I: Effect of laser beam travelling speed on microstructural features and surface hardness. *Am. J. Eng. Appl. Sci.* **2013**, *6*, 352–359. [CrossRef]
5. Kröpfl, O.; Vöhringer, E.; Macherauch, E. Creep Behavior of Dispersion-Hardened Aluminum Materials. *Mech. Time-Depend. Mat.* **1999**, *3*, 1–13. [CrossRef]
6. Stobrawa, Z.M.; Rdzawski, W.; Głuchowski, W. Structure and properties of dispersion hardened submicron grained copper. *J. Ach. Mat. Manuf. Eng.* **2007**, *20*, 195–198.
7. Berezovsky, V.V.; Shavnev, A.A.; Lomov, S.B.; Kurganova, Y.A. Obtaining and analysis of the structure of dispersion-strengthened composite materials of the Al-SiC system with different content of the reinforcing phase. *Avia. Mat. Tech.* **2014**, *6*, 17–23. [CrossRef]
8. Boopathi, M.M.; Arulshri, K.P.; Iyandurai, N. Evaluation of Mechanical Properties of Aluminium Alloy 2024 Reinforced with Silicon Carbide and Fly Ash Hybrid Metal Matrix Composites. *Am. J. Appl. Sci.* **2013**, *10*, 219–229. [CrossRef]
9. Lutz, A.R.; Galochkina, I.A. *Aluminum Composite Alloys—Alloys of the Future: Educational Book*; Samara State Technical University: Samara, Russia, 2013; p. 82. (In Russian)
10. Kaldre, I.; Bojarevičs, A.; Grantsa, I.; Beinerts, T.; Kalvāns, M.; Milgrāvis, M.; Gerbeth, G. Nanoparticle dispersion in liquid metals by electromagnetically induced acoustic cavitation. *Acta. Mater.* **2016**, *118*, 253–259. [CrossRef]
11. Wang, G.; Wang, Q.; Easton, M.A.; Dargusch, M.S.; Qian, M.; Eskin, D.G.; StJohn, D.H. Role of ultrasonic treatment, inoculation and solute in the grain refnement of commercial purity aluminium. *Sci. Rep.* **2017**, *7*, 9729. [CrossRef] [PubMed]
12. Valiev, R.Z.; Estrin, Y.; Horita, Z.; Langdon, T.G.; Zehetbauer, M.J.; Zhu, Y. Producing bulk ultrafine-grained materials by severe plastic deformation: Ten years later. *JOM* **2016**, *68*, 1216. [CrossRef]
13. Zha, M.; Li, Y.; Mathiesen, R.H.; Bjørge, R.; Roven, H.J. Microstructure evolution and mechanical behavior of a binary Al–7Mg alloy processed by equal-channel angular pressing. *Acta Mater.* **2015**, *84*, 42–54. [CrossRef]
14. Sunghak, L.; Dongil, K.; Dongwoo, S. Microstructure and fracture of SiC-particulate-reinforced cast A356 aluminum alloy composites. *Metall. Mater. Trans.* **1996**, *27*, 3893–3901. [CrossRef]

15. Vorozhtsov, S.; Zhukov, I.; Promakhov, V.; Naydenkin, E.; Khrustalyov, A.; Vorozhtsov, A. The Influence of ScF3 Nanoparticles on the Physical and Mechanical Properties of New Metal Matrix Composites Based on A356 Aluminum Alloy. *JOM* **2016**, *68*, 3101–3106. [CrossRef]
16. Khmeleva, M.; Khrustalev, A.; Vorozhtsov, A. Structure and mechanical properties of A356-C alloys. *MATEC Web Conf.* **2018**, *243*, 24. [CrossRef]
17. Vorozhtsov, A.B.; Platov, V.V.; Kozulin, A.A.; Khrustalev, A.P.; Mishin, I.P.; Zhukov, I.A. Study of the effect of TiB2 particles on the structure, deformation behavior, and properties of the aluminum alloy 1550. *Vestn. Tomsk. Gos. Univ. Mat. Mekh.* **2020**, *67*, 102–116. [CrossRef]
18. Stewart, A.T.; Martin, J.W. Dislocation-particle interactions in plastically deformed two-phase aluminium crystals. *Acta Metall.* **1975**, *23*, 1–7. [CrossRef]
19. Hymphreys, F.J.; Hirsch, P.B. The deformation of single crystals of copper and copper-zinc alloys containing alumina particles—II. Microstructure and dislocation-particle interactions. *Pros. Roy. Soc. Lond.* **1970**, *A318*, 73–92. [CrossRef]
20. Orowan, E. Condition for dislocation passage of precipitations. *Proc. Symp. Intern. Stress Met. Alloy.* **1948**, *VIII*, 451–454.
21. Ashby, M.F. Work hardening of dispersion-hardened crystals. *Phil. Mag.* **1966**, *14*, 1157–1178. [CrossRef]
22. Ebeling, R.; Ashby, M.F. Dispersion hardening of copper single crystals. *Phil. Mag.* **1966**, *13*, 805–834. [CrossRef]
23. Hazzledine, P.M.; Hirsch, P.B. A coplanar Orowan loops model for dispersion hardening. *Phil. Mag.* **1974**, *30*, 1331–1351. [CrossRef]
24. Hymphreys, F.J.; Martin, J.W. The effect of dispersed phases upon dislocation distributions in plastically deformed copper crystals. *Phil. Mag.* **1967**, *16*, 927–957. [CrossRef]
25. Ashby, M.F.; Johnson, K. Materials and Design. In *The Art and Science of Materials Selection in Product Design*; Butterworth Heinemann: Oxford, UK, 2002; p. 336.
26. Kovalevskaya, T.A.; Daneyko, O.I. Formation of maximum strength of disperse-strengthened aluminum-based crystalline alloys containing incoherent particles. *Bullet. Rus. Acad. Scien. Phys.* **2021**, *85*, 1002–1007. (In Russian) [CrossRef]
27. Daneyko, O.I.; Kovalevskaya, T.A. Temperature Effect on Stress-Strain Properties of Dispersion-Hardened Crystalline Materials with Incoherent Nanoparticles. *Russ. Phys. J.* **2019**, *61*, 1687–1694. [CrossRef]
28. Kovalevskaya, T.A.; Daneyko, O.I. The Influence of Scale Parameters of Strengthening Phase on Plastic Shear Zone in Heterophase Alloys with Incoherent Nanoparticles. *Russ. Phys. J.* **2020**, *62*, 2247–2254. [CrossRef]
29. Daneyko, O.I.; Kovalevskaya, T.A.; Matvienko, O.V. The influence of incoherent nanoparticles on thermal stability of aluminum alloys. *Russ. Phys. J.* **2018**, *61*, 1229–1235. [CrossRef]
30. Matvienko, O.V.; Daneyko, O.I.; Kovalevskaya, T.A. Stress-Stain State of Pipe Made of Copper-Based Alloy Strengthened with Incoherent Nanoparticles. *Russ. Phys. J.* **2017**, *60*, 562–569. [CrossRef]
31. Matvienko, O.V.; Daneyko, O.I.; Kovalevskaya, T.A. Dislocation Structure of the Pipe Made of Alloy Reinforced with Incoherent Particles Under Uniform Internal Pressure. *Russ. Phys. J.* **2017**, *60*, 1233–1242. [CrossRef]
32. Matvienko, O.; Daneyko, O.; Kovalevskaya, T.; Khrus talyov, A.; Zhukov, I.; Vorozhtsov, A. Investigation of stresses induced due to the mismatch of the coefficients of thermal expansion of the matrix and the strengthening particle in aluminum-based composites. *Metals* **2021**, *11*, 279. [CrossRef]
33. Birger, I.A.; Koterov, N.I. *Strength Calculation of Aircraft Gas Turbine Engines*; M: Mashinostroenie: Moscow, Russia, 1984; p. 208. (In Russian)
34. Demyanushko, I.V.; Koroleva, E.F. Optimal design of turbomachinery disks. *Izv. AN USSR* **1972**, *2*, 176–180. (In Russian)
35. Demyanushko, I.V.; Birger, I.A. *Calculation of the Strength of Rotating Disks*; M: Mashinostroenie: Moscow, Russia, 1978; p. 247. (In Russian)
36. Malinin, N.N. Calculation of a rotating unevenly heated disc of variable thickness. *Inz. Sb.* **1953**, *17*, 151–163.
37. Gamer, U. Tresca's Yield Condition and the Rotating Disk. *J. Appl. Mech.* **1983**, *50*, 676–678. [CrossRef]
38. Artemov, M.A.; Yakubenko, A.P. Rotating disc mechanical behaviour mathematical modelling. *Proc. Voron. State Univ. Ser. Phys. Math.* **2014**, *1*, 30–38.
39. Lomakin, E.; Alexandrov, S.; Jeng, Y.R. Stress and strain fields in rotating elastic/plastic annular discs. *Arch. Appl. Mech.* **2016**, *86*, 235–244. [CrossRef]
40. Timoshenko, S.; Goodier, J.; Abramson, H. Theory of Elasticity (3rd ed.). *J. Appl. Mech.* **1970**, *37*, 888. [CrossRef]
41. Boresi, A.P.; Schmidt, R.J.; Sidebottom, O.M. *Advanced Mechanics of Materials*, 5th ed.; John Wiley & Sons: New York, NY, USA, 1993.
42. Chakrabarty, J. *Theory of Plasticity*, 3rd ed.; Elsevier: Amsterdam, The Netherlands, 2006.
43. Gamer, U. Elastic-plastic deformation of the rotating solid disk. *Ing. Arch.* **1984**, *54*, 345–354. [CrossRef]
44. Jahromi, B.H.; Nayeb-Hashemi, H.; Vaziri, A. Elasto-plastic stresses in a functionally graded rotating disk. *J. Eng. Mat. Tech.* **2012**, *134*, 021004. [CrossRef]
45. Apatay, T.; Eraslan, A.N. Elastic deformation of rotating parabolic discs: Analytical solutions. *J. Fac. Eng. Arch. Gazi Univ.* **2003**, *18*, 115–135.
46. Calderale, P.M.; Vivio, F.; Vullo, V. Thermal stresses of rotating hyperbolic disks as particular case of non-linearly variable thickness disks. *J. Therm. Stress.* **2012**, *35*, 877–891. [CrossRef]

47. Güven, U. Tresca's yield condition and the linear hardening rotating solid disk of variable thickness. *J. Appl. Mat. Mech.* **1995**, *75*, 805–807. [CrossRef]
48. Vivio, F.; Vullo, V.; Cifani, P. Theoretical stress analysis of rotating hyperbolic disk without singularities subjected to thermal load. *J. Therm. Stress.* **2014**, *37*, 117–136. [CrossRef]
49. Eraslan, A.N. Elastoplastic deformations of rotating parabolic solid disks using Tresca's yield criterion. *Eur. J. Mech. A/Solids* **2003**, *22*, 861–874. [CrossRef]
50. Eraslan, A.N. Elastic–plastic deformations of rotating variable thickness annular disks with free, pressurized and radially constrained boundary conditions. *Int. J. Mech. Sci.* **2003**, *45*, 643–667. [CrossRef]
51. Yıldırım, V. A Parametric Study on the Centrifugal Force-Induced Stress and Displacements in Power-Law Graded Hyperbolic Discs. *Lat. Am. J. Solids Struct.* **2018**, *15*, e34. [CrossRef]
52. Thakur, P. Analysis of stresses in a thin rotating disc with inclusion and edge loading. *Sci. Technol. Rev.* **2013**, *63*, 9–16.
53. Aleksandrova, N.N.; Artemov, M.A.; Baranovskii, E.S.; Shashkin, A.I. On stress/strain state in a rotating disk. *J. Phys. Conf. Ser.* **2019**, *1203*, 012001. [CrossRef]
54. Aleksandrova, N. Application of Mises yield criterion to rotating solid disk problem. *Int. J. Eng. Sci.* **2012**, *51*, 333–337. [CrossRef]
55. Aleksandrova, N. Exact deformation analysis of a solid rotating elastic-perfectly plastic disk. *Int. J. Mech. Sci.* **2014**, *88*, 55–60. [CrossRef]
56. Afsar, A.M.; Go, J. Finite element analysis of thermoelastic field in a rotating FGM circular disk. *Appl. Math. Mod.* **2010**, *34*, 3309–3320. [CrossRef]
57. Lamb, H.; Southwell, R.V. The vibrations of a spinning disk. *Proc. R. Soc. Ser. A* **1921**, *99*, 272–280. [CrossRef]
58. Matvienko, O.V.; Daneyko, O.I.; Kovalevskaya, T.A. Residual Stresses Induced by Elastoplastic Unloading in a Tube Made of Dispersion-Hardened Alloy. *Russ. Phys. J.* **2018**, *61*, 730–742. [CrossRef]
59. Matvienko, O.V.; Daneyko, O.I.; Kovalevskaya, T.A. Strengthening Particle Size Effect on Residual Stresses in Dispersion-Hardened Alloy. *Russ. Phys. J.* **2018**, *61*, 962–973. [CrossRef]
60. Matvienko, O.V.; Daneyko, O.I.; Kovalevskaya, T.A. Elastoplastic Deformation of Dispersion-Hardened Aluminum Tube Under External Pressure. *Russ. Phys. J.* **2018**, *61*, 1520–1528. [CrossRef]
61. Matvienko, O.; Daneyko, O.; Kovalevskaya, T. Mathematical modeling of nanodispersed hardening of FCC materials. *Acta Met. Sin.* **2018**, *31*, 1297–1304. [CrossRef]
62. Matvienko, O.; Daneyko, O.; Kovalevskaya, T. Mathematical modeling of plastic deformation of a tube from dispersion-hardened aluminum alloy. *MATEC Web Conf.* **2018**, *243*, 8. [CrossRef]
63. Matvienko, O.; Daneyko, O.; Kovalevskaya, T. Mathematical modeling of plastic deformation of a tube from dispersion-hardened aluminum alloy in an inhomogeneous temperature field. *Crystals* **2020**, *10*, 1103. [CrossRef]
64. Matvienko, O.; Daneyko, O.; Kovalevskaya, T. Investigation of the influence of temperature distribution on the stress-strain state of the tube walls made from a disperse-hardened alloy. *Bas. Prob. Mat. Sci.* **2020**, *17*, 330–337. [CrossRef]
65. Zhukov, I.A.; Promakhov, V.V.; Matveev, A.E.; Platov, V.V.; Khrustalev, A.P.; Dubkova, Y.A.; Vorozhtsov, S.A.; Potekaev, A.I. Principles of structure and phase composition formation in composite master alloys of the Al–Ti–B/B4c systems used for aluminum alloy modification. *Russ. Phys. J.* **2018**, *60*, 2025–2031. [CrossRef]
66. Vorozhtsov, S.; Minkov, L.; Dammer, V.; Khrustalyov, A.; Zhukov, I.; Promakhov, V.; Vorozhtsov, A.; Khmeleva, M. Ex-situ introduction and distribution of nonmetallic particles in aluminum melt: Modeling and experiment. *JOM* **2017**, *69*, 2653–2657. [CrossRef]
67. Vencl, A.; Bobić, I.; Stanković, M.; Hvizdoš, P.; Bobić, B.; Stojanović, B.; Franek, F. Influence of secondary phases in A356 MMCs on their mechanical properties at macro-and nanoscale. *J. Brazil. Soc. Mech. Sci. Eng.* **2020**, *42*, 1–12. [CrossRef]
68. Wang, Q.G.; Caceres, C.H.; Griffiths, J.R. Damage by eutectic particle cracking in aluminum casting alloys A356/357. *Met. Mater. Trans. A* **2003**, *34*, 2901–2912. [CrossRef]
69. Ma, S.; Wang, X. Mechanical properties and fracture of in-situ Al3Ti particulate reinforced A356 composites. *Mat. Sci. Eng. A* **2019**, *754*, 46–56. [CrossRef]
70. Wang, M.; Chen, D.; Chen, Z.; Wu, Y.; Wang, F.; Ma, N.; Wang, H. Mechanical properties of in-situ TiB2/A356 composites. *Mat. Sci. Eng. A* **2014**, *590*, 246–254. [CrossRef]
71. Königshofer, R.; Fürnsinn, S.; Steinkellner, P.; Lengauer, W.; Haas, R.; Rabitsch, K.; Scheerer, M. Solid-state properties of hot-pressed TiB2 ceramics. *Int. J. Refr. Met. Hard Mat.* **2005**, *23*, 350–357. [CrossRef]
72. Wang, H.Y.; Xue, F.Y.; Zhao, N.H.; Li, D.J. First-principles calculation of elastic properties of TiB2 and ZrB2. *Adv. Mat. Res.* **2011**, *150*, 40–43. [CrossRef]
73. Voitenko, A.F.; Skripnik, Y.D.; Solov'eva, N.G. Anisotropy of elasticity characteristics for a series of structural metals in the temperature from 4.2 to 300 °K. *Strength Mat.* **1987**, *19*, 89–92. [CrossRef]
74. Khrustalyov, A.P.; Kakhize, N.I.; Platov, V.V.; Zhukov, I.A.; Vorozhtsov, A.B. Influence of Tungsten Nanoparticles on Microstructure and Mechanical Properties of an Al-5% Mg Alloy Produced by Casting. *Metals* **2022**, *12*, 989. [CrossRef]
75. Aguiar, L.R.C.; Carneiro, S.H.S.; Paiano, S. Modal analysis of a satellite with different materials. *Rev. Interdiscip. Pesqui. Eng.* **2017**, *2*, 186–198.
76. Zhang, X.; Jiang, W. First-principles investigation on vibrational, anisotropic elastic and thermodynamic properties for L12structure of Al3Er and Al3Yb under high pressure. *Philos. Mag.* **2016**, *96*, 320–348. [CrossRef]

77. Tang, Z.; Cui, J.; Yu, M.; Zhu, W.; Xu, Z.; Zeng, J.; Xu, T.; Yang, H.; Tan, Y.; Yang, B. A new insight on the diffusion growth mechanism of intermetallic compounds in Al-Er system. *Mat. Des.* **2022**, *224*, 111341. [CrossRef]
78. Ishlinskiy, A.Y.; Ivlev, D.D. *Mathematical Theory of Plasticity*; Fizmatlit: Moscow, Russia, 2003; p. 704.
79. Matvienko, O.V.; Daneyko, O.I.; Kovalevskaya, T.A. Elastoplastic Deformation of Dispersion-Hardened Aluminum Tube Under External and Internal Pressure. *Russ. Phys. J.* **2019**, *62*, 720–728. [CrossRef]
80. Yu, M.H. References and Bibliography. In *Unified Strength Theory and Its Applications*; Springer: Berlin/Heidelberg, Germany, 2018; pp. 371–460. [CrossRef]
81. Matvienko, O.V.; Daneyko, O.I.; Kovalevskaya, T.A. Stress-strain State of Dispersion-hardened Aluminum Tube Under External and Internal Pressure. *Russ. Phys. J.* **2020**, *62*, 1805–1812. [CrossRef]
82. Timoshenko, S.P.; Goodier, J.N. *Theory of Elasticity*; Mcgraw Hill: New York, NY, USA, 2010.
83. Matvienko, O.V.; Daneyko, O.I.; Kovalevskaya, T.A. A Study of residual stress formation after elastoplastic deformation of pipe walls, made from disperse-hardened aluminum alloy, as a result of external pressure. *Tomsk St. Univ. J. Math. Mech.* **2021**, *72*, 102–117. [CrossRef]
84. Gorhkov, A.G.; Starovoitov, E.I.; Tarlakovsky, D.V. *Theory of Elasticity and Plasticity*; Fizmatlit: Moscow, Russia, 2002; p. 416. (In Russian)
85. Matvienko, O.V.; Daneyko, O.I.; Kovalevskaya, T.A. Stress-Strain State of Disperse-Hardened Aluminum Joint Tube Under Internal Pressure. *Russ. Phys. J.* **2020**, *63*, 779–790. [CrossRef]

Disclaimer/Publisher's Note: The statements, opinions and data contained in all publications are solely those of the individual author(s) and contributor(s) and not of MDPI and/or the editor(s). MDPI and/or the editor(s) disclaim responsibility for any injury to people or property resulting from any ideas, methods, instructions or products referred to in the content.